

**Key Points:**

- Remote equatorial forcing explains more than 70% of the interannual sea level variability off the northern coast of the Gulf of Guinea
- The oceanic connection with the equatorial variability is propagative, taking ~ 1.5 months to affect the coastal variability off Liberia
- Remotely-forced sea surface temperature anomaly is only significant in the Ivorian-Ghanaian upwelling system and is seasonally modulated

Supporting Information:

Supporting Information may be found in the online version of this article.

Correspondence to:

S. Illig,
serena.illig@ird.fr

Citation:

Illig, S., Djakouré, S., & Mitchodigni, T. (2024). Influence of the remote equatorial dynamics on the interannual variability along the northern coast of the Gulf of Guinea. *Journal of Geophysical Research: Oceans*, 129, e2024JC021011. <https://doi.org/10.1029/2024JC021011>

Received 9 FEB 2024

Accepted 21 JUL 2024

Author Contributions:

Conceptualization: Serena Illig

Data curation: Serena Illig,
Toussaint Mitchodigni

Formal analysis: Serena Illig

Supervision: Serena Illig,
Sandrine Djakouré




Validation: Serena Illig,
Toussaint Mitchodigni

Visualization: Serena Illig,
Toussaint Mitchodigni

Writing – original draft: Serena Illig,
Sandrine Djakouré

Writing – review & editing: Serena Illig,
Sandrine Djakouré

Influence of the Remote Equatorial Dynamics on the Interannual Variability Along the Northern Coast of the Gulf of Guinea

Serena Illig^{1,2} , Sandrine Djakouré³ , and Toussaint Mitchodigni^{4,5} 

¹Laboratoire d'Etudes en Géophysique et Océanographie Spatiale (LEGOS), CNRS/IRD/UT3/CNES, Toulouse, France, ²Department of Oceanography, University of Cape Town, Cape Town, South Africa, ³Laboratory of Matter, Environmental and Solar Energy Sciences (LASMES), Ocean-Atmosphere Interaction Group, University Félix Houphouët-Boigny, Abidjan, Côte d'Ivoire, ⁴Department of Oceanography and Applications, International Chair in Mathematical Physics and Applications, University of Abomey-Calavi, Cotonou, Benin, ⁵Institut de Recherches Halieutiques et Océanologiques du Bénin, Cotonou, Benin

Abstract This study explores the oceanic connection between the equatorial dynamics and the coastal variability along the northern coast of the Gulf of Guinea on interannual timescales, based on experiments with a high-resolution tropical Atlantic Ocean model over 1958–2015. Equatorial Kelvin waves, forced by wind-stress anomalies in the west-central equatorial basin, significantly control the interannual fluctuations of the coastal sea-level and subsurface temperature near the thermocline ($>70\%$), leaving only a marginal role for the local forcing contribution. The dynamical coastal response exhibits a clear propagative nature, with poleward propagations ($0.75\text{--}1.2\text{ m.s}^{-1}$) from Cameroon to Liberia. Because the northern coast of the Gulf of Guinea is close to the equatorial waveguide, the coastal variability is influenced by both equatorially-forced coastal trapped waves and reflected equatorial Rossby waves. Furthermore, remote equatorial forcing explains more of the surface temperature variance for the coastal systems associated with clear upwelling characteristics such as Côte d'Ivoire and Ghana, where subsurface/surface coupling is more efficient. The surface thermal amplitude and timing is shaped by the coastal stratification and circulation and exhibits a marked seasonal modulation, so that the timing of the Sea Surface Temperature (SST) anomalies relative to the dynamical signature lacks consistency, making SST a less reliable variable for tracking coastal propagations in the Gulf of Guinea. Our findings open the possibility of predicting interannual changes in coastal conditions off Côte d'Ivoire and Ghana a few months in advance, to anticipate impacts on fish habitats and resources, and to facilitate proactive measures for sustainable management and conservation efforts.

Plain Language Summary Our study explores the interannual fluctuations of the oceanic conditions along the northern coast of the Gulf of Guinea using numerical experiments conducted with an ocean model of the tropical Atlantic at high-resolution. Modeling results show that the coastal interannual variability of sea level and subsurface temperature is driven to a large extent ($>70\%$) by the propagation of oceanic long waves forced distantly in the western central equatorial basin by a modulation of the trade winds. A clear propagative signal is detected along the northern coast of the Gulf of Guinea, which takes about 1.5 months to affect the coastal variability off Liberia. In contrast, coastal surface winds and atmospheric fluxes have only a marginal influence on the coastal variability on interannual timescales. Furthermore, the impact on the sea surface temperature is only substantial and seasonal along the coasts of Côte d'Ivoire and Ghana, where the upwelling dynamics favors an efficient penetration of the subsurface temperature anomalies into the surface layer. This oceanic connection unveils the potential for predicting fluctuations in coastal conditions and fish habitats in the Ivorian-Ghanaian upwelling system several months in advance, for sustainable resource management.

1. Introduction

The Gulf of Guinea (GoG) hosts two major upwelling regions. The largest and most intense is located in the eastern equatorial basin, and the second is the coastal Ivorian-Ghanaian upwelling system (Brandt et al., 2023; Longhurst, 1993). They are subject to a pronounced seasonal cycle (Figure 1), characterized by the development of a cold tongue along the equator in the boreal spring (Burls et al., 2011; Ding et al., 2009; Xie & Carton, 2004) and fluctuations along the coast of the Northern Gulf of Guinea (NGG, Alory et al., 2021; Brandt et al., 2023; Djakouré et al., 2017; Sohoun et al., 2020; Topé et al., 2023). Morlière (1970) described the seasonal cycle of the

© 2024. The Author(s).

This is an open access article under the terms of the [Creative Commons Attribution-NonCommercial-NoDerivs License](#), which permits use and distribution in any medium, provided the original work is properly cited, the use is non-commercial and no modifications or adaptations are made.

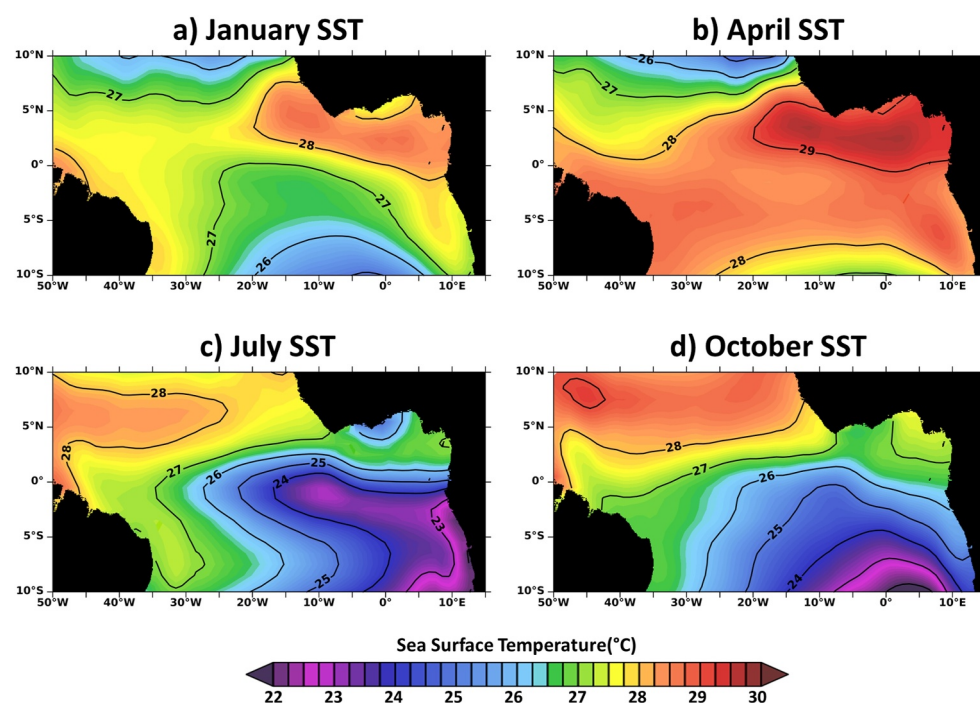


Figure 1. Monthly climatological Sea Surface Temperature (SST, °C) from weekly Optimum Interpolation SST (Huang et al., 2021) in (a) January, (b) April, (c) July, and (d) October. Data are averaged between 1982 and 2015.

Sea Surface Temperature (SST) off Abidjan (Côte d'Ivoire) and identified four main marine seasons associated with fluctuations in coastal upwelling: (a) a minor cold season (*la Petite Saison Froide*) from January to March (Figure 1a); (b) a major warm season from March to June (Figure 1b), followed by a transition season from June to July with a gradual decrease in SST; (c) a major cold season from July–September to early October (*la Grande Saison Froide*, see Figure 1c); and (d) a major warm season from November to December (Figure 1d). Enhanced productivity during the upwelling seasons sustains fisheries production and socioeconomic activities off the NGG coasts (Amemou et al., 2020; Koné et al., 2017). Seasonal SST variations in the GoG, on the order of 5°C, are favored by the shallow thermocline (Djakouré et al., 2014) and its proximity to the surface mixed layer. They largely inflect the onset and amplitude of the African monsoon (Caniaux et al., 2011; de Coëtlogon et al., 2023; Kouadio et al., 2013).

The climatological mean state of the ocean currents, temperature, and sea level in the GoG is modulated on interannual timescales (Foltz et al., 2019; Hardman-Mountford & McGlade, 2003; Lübbecke, 2013; Marin et al., 2009; Xie & Carton, 2004). The year-to-year SST variations, albeit less marked than the seasonal fluctuations, hover around 1.5–2°C (Da-Allada et al., 2021; Hardman-Mountford & McGlade, 2003; Lübbecke, 2013; Toualy et al., 2012). In the cold tongue region, the interannual variability is predominantly associated with the Atlantic Niño basin mode (e.g., Carton & Huang, 1994; Illig et al., 2006; Lübbecke et al., 2018; Ruiz-Barradas et al., 2000; Servain et al., 2000; Zebiak, 1993). The ocean dynamics resembles that of El-Niño Southern Oscillation in the Pacific Ocean, with a weaker amplitude (Keenlyside & Latif, 2007). It is associated with a modulation of the zonal trade winds in the west-central basin, to which the ocean adjusts through the propagation of eastward-propagating long Equatorial Kelvin Waves (EKW, Clarke, 1983; Illig et al., 2004, 2020; Philander, 1990). Upon reaching the Gabonese coast, part of their energy is reflected back toward the center of the basin into westward-propagating Equatorial Rossby Waves (ERWs). Notably, due to the proximity of the NGG coastlines to the equator, ERWs extend up to the coast, causing a deformation of their meridional structures (Cane & Sarachik, 1979; Illig et al., 2004). These long waves trigger significant changes in the vertical and horizontal currents, resulting in strong subsurface temperature anomalies near the thermocline and potentially leading to the development of extreme Atlantic Niño/Niña events during the boreal spring/summer (Burmeister et al., 2016; Foltz & McPhaden, 2010; Illig et al., 2006, 2020; Martín-Rey & Lazar, 2019).

Notably, a significant part of the incident EKW energy is also transmitted poleward along the west African coast as Coastal Trapped Waves (CTWs, Brink, 1982; Clarke, 1983; Clarke & Brink, 1985; Illig, Bachèlery, & Cadier, 2018; Illig, Cadier, et al., 2018; Moore, 1968). They establish an ocean connection with the equatorial variability that affects the coastal dynamics very far from the equatorial waveguide, as far as the southern tip of Africa in the Southern Hemisphere (Bachèlery et al., 2020; Illig & Bachèlery, 2019). At interannual frequencies, this equatorial connection, with phase speeds ranging from 0.8 to 1.1 m.s⁻¹, accounts for up to 89% of the interannual coastal Sea Level Anomalies (SLAs, Bachèlery et al., 2016a) and is essential for the development of extreme warm and cold events off Angola and Namibia (Benguela Niños/Niñas, Bachèlery et al., 2016a, 2020; Illig & Bachèlery, 2024; Illig et al., 2020; Rouault et al., 2007, 2018). In the NGG, the control of the coastal ocean variability by the equatorial linear dynamics has been reported on submonthly (Clarke & Battisti, 1983; Picaut & Verstraete, 1979) and subseasonal (Polo et al., 2008) timescales, with phase speeds ranging from 1.5 to 2.1 m.s⁻¹. The connection with the equatorial variability has also been suggested to explain the seasonal cooling of the NGG coastal SST (Picaut, 1983), but this mechanism remains uncertain (Djakouré et al., 2017). While the coastal band along the NGG coast also experiences substantial interannual variability (Da-Allada et al., 2021; Hardman-Mountford & McGlade, 2003; Merle et al., 1979; Sohoul et al., 2020), the underlying forcing mechanisms are not yet fully understood and the connection with the equatorial variability has not been thoroughly examined. Indeed, these studies have reported several warm and cold coastal events from remote-sensed observations, in situ measurements, and ocean models, associated with changes in horizontal and vertical advections (Da-Allada et al., 2021). These SST fluctuations, with anomalies deviating from climatological conditions by up to 2°C, are more pronounced in the western NGG region, off Côte d'Ivoire and Ghana, than in the eastern coastal band, off Benin and Nigeria (Sohoul et al., 2020). They influence regional precipitations (Ali et al., 2011; Brandt et al., 2011; Fontaine & Janicot, 1992; Lamb, 1978; Lamb & Pepler, 1992; Mohino et al., 2011; Rodríguez-Fonseca et al., 2015; Vizy & Cook, 2001), as well as primary production, pelagic fish habitat, and marine resource abundance (Binet & Marchal, 1993; Binet & Servain, 1993).

A first examination of the interannual sea level derived from altimetric observations (Pujol et al., 2016) along the equatorial and NGG coastal waveguides (Figure 2a) reveals a strong coherence between the equatorial fluctuations and the coastal SLA along the coasts of Cameroon, Nigeria, Benin, Togo, Ghana, Côte d'Ivoire, and Liberia (Figure 2b). Additionally, the coastal signal shows propagative characteristics, suggesting an efficient EKW/CTW dynamics. However, in remote-sensed SST (Huang et al., 2021), the continuation of the interannual equatorial signal along the NGG coastal band appears less obvious, but some connections stand out, such as in 2004, 2005, 2010, and 2012 for instance (Figure 2c). These particular coastal events have been reported in previous studies (Da-Allada et al., 2021; Djakouré et al., 2014, 2017; Lefèvre et al., 2013; Marin et al., 2009; Sohoul et al., 2020) but not in relation with the equatorial connection. Following on from these previous studies, the aim of this paper is to document and quantify the link between equatorial linear dynamics and coastal variability along the NGG coasts on interannual timescales. Our methodology is based on experiments with a regional model of the tropical Atlantic, applying the methods developed for the study of the remote forcing along the southwest coast of Africa (Bachèlery et al., 2016a, 2020; Illig et al., 2020). The paper is organized as follows: In Section 2, we introduce the tropical Atlantic Ocean model configurations and present a set of model experiments. A validation exercise of the model is provided in Text S1 in Supporting Information S1. Section 3 shows strong evidence of interannual equatorially-forced propagation along the northern coast of the Gulf of Guinea. Section 4 provides a summary of our results, followed by a discussion, and concluding remarks.

2. Methodology

The methodology is based on the analysis of the outputs of a regional ocean model of the tropical Atlantic, focusing on the interannual variability in the GoG. We use the 58-year long simulation of Illig et al. (2020) and perform a sensitivity experiment to quantify the contribution of the equatorial remote forcing to the coastal variability in the NGG. Idealized experiments, in which interannual equatorial waves are triggered, allow us to track the long wave propagation along the NGG coastline and to assess the role of the coastal seasonal stratification on the equatorial connection.

2.1. Ocean Model Configuration and CROCO^{REF} Simulation

We use the Coastal and Regional Ocean COMMunity model (CROCO, Auclair et al., 2022; Debreu et al., 2012) tropical Atlantic Ocean model configuration developed by Illig et al. (2020). It spans from the Americas to Africa

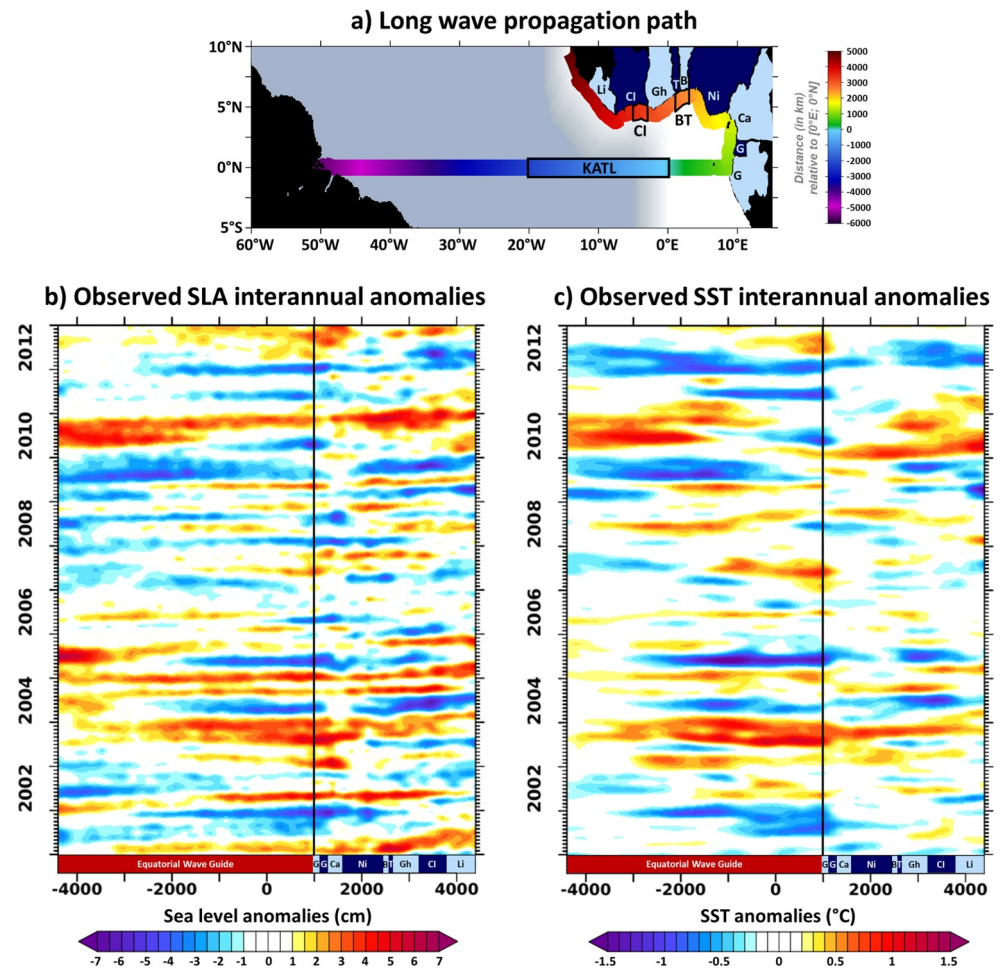


Figure 2. (a) Map of the region of interest emphasizing the 1°-wide pathway where equatorial Kelvin waves cross the Atlantic basin and give rise to subsequent coastal trapped wave propagations along the coasts of Gabon, Equatorial Guinea, Cameroon, Nigeria, Benin, Togo, Ghana, Côte d'Ivoire, and Liberia. The colors in the polytube represent the distance (in km) from [0°E; 0°N]. The black boxes indicate the KATL region (20°W–0°E, 0.5°S–0.5°N), as well as the coastal boxes off Benin-Togo (BT, 1°E–3°E) and Côte d'Ivoire (CI, 5°W–3°W). The gray-blue shading delineates the region where the interannual forcing is restricted in the CROCO^{REMOTE} sensitivity experiments (see Section 2.2). (b, c) Hovmöller diagrams of observed 2001–2012 Sea level interannual Anomalies (SLAs, in cm, from altimetric AVISO data (Pujol et al., 2016)) and sea surface temperature interannual Anomalies (SSTAs, in °C, from weekly OISST maps (Huang et al., 2021)), respectively, along the pathway of equatorial and coastal wave propagations (x-axis). Anomalies are computed over the period 1993–2015.

(62.25°W to 17.25°E) from 30°S to 10°N, at a 1/12° horizontal resolution and with 37 terrain-following vertical levels. The northern and southern open lateral boundaries remain climatological (CARS2009, Dunn, 2009; Ridgway et al., 2002). We start by analyzing the multidecadal (1958–2015) realistic simulation of Illig et al. (2020), in which the model is forced by momentum, heat, and freshwater surface fluxes estimated with bulk formulas using the daily averaged surface fields from the DRAKKAR Forcing Set v5.2 (Dussin et al., 2016). Note that an analytical diurnal cycle modulates the shortwave radiation, and sea surface salinity is restored to the CARS2009 monthly climatological values to account for river runoffs. The reader is referred to Illig et al. (2020) for a detailed description of the model setup. This simulation, hereafter referred to as CROCO^{REF}, has been previously used to study the coastal dynamics along the southwestern coast of Africa on seasonal (Körner et al., 2024), interannual (Illig et al., 2020), and decadal (Tomety et al., 2024) timescales. In this study, we examine 3-day averages of wind-stress, temperature, currents, sea level, and Mixed-Layer Depth (MLD) to comprehend the interannual coastal dynamics in the NGG. The MLD is derived from the turbulent mixing scheme (K-profile parameterization, Large et al., 1994), while the thermocline position is estimated offline where the

thermal stratification is maximum. Extensive validation of the model configuration can be found in Illig et al. (2020). Specific comparisons with remotely-sensed SLA and interannual SST anomalies (SSTAs) show that the east-equatorial and coastal interannual variability off the NGG are realistically represented in CROCO^{REF} (see Text S1 and Figures S1 and S2 in Supporting Information S1).

2.2. Interannual Anomalies and Key Regions

The interannual variability is estimated as in Illig et al. (2020). First, monthly anomalies are computed by estimating monthly means and subtracting the monthly climatological mean state. The decadal contribution is filtered out using a high-pass Fast Fourier Transform filter with a cutoff frequency of 10 year⁻¹. Subseasonal fluctuations are also removed by applying a 1-2-1 running weighted average. The resulting monthly time series is then interpolated back to the original temporal resolution using cubic splines.

In the following, we focus on the dynamics along the equatorial waveguide (within the 0.5°S–0.5°N equatorial band) and in the 1°-wide coastal margin along the northern coast of the GoG (see colored polytube in Figure 2a). In the eastern equatorial Atlantic, strong equatorial wave propagations are identified by averaging the interannual SLA within the KATL box (Equatorially-trapped Kelvin wave domain [20°W–0°E; 0.5°S–0.5°N], see Figure 2a). Along the NGG coast, we zoom in on two regions that undergo distinct dynamics: (a) the 1°-wide coastal band off Benin-Togo (BT, [1°E–3°E]) and (b) the 1°-wide coastal band off eastern Côte d'Ivoire (CI, [5°W–3°W]).

2.3. Sensitivity and Idealized Experiments

To disentangle the effect of local atmospheric forcing from the effect of the remote ocean connection with the linear equatorial variability on the interannual variability of the NGG, we conducted a sensitivity experiment with the CROCO model. In CROCO^{REMOTE}, the model is forced by the surface wind-stress from CROCO^{REF} and uses the same heat and freshwater bulk formula input fields, but the interannual variability in these fields is restricted to the western equatorial basin within 10°S–10°N, away from the NGG coastal band (see gray-blue shading in Figure 2a). Note that, to reduce spurious horizontal gradients in the forcing, a gradual (linear) transition zone of 5° width is added to the south and east between the region where interannual variability is filtered out and the region where the forcing remains identical to CROCO^{REF}s. This simulation is run from 1958 to 2015, starting after CROCO^{REF} 5-year spin-up. Assuming some linearity, this sensitivity experiment allows us to quantify the fraction of the NGG coastal interannual variability that is controlled by the ocean connection with the equatorial linear dynamics (see Section 3.2), as in Bachèlery et al. (2020) for the Angola-Benguela upwelling system. In particular, we compute Pearson correlation coefficients using the outputs of CROCO^{REF} and CROCO^{REMOTE}. To assess their statistical significance at a confidence level of 99%, we use the methodology of Scirrenammano (1979) and employ a Student *t*-test, adjusting the degrees of freedom to account for the temporal autocorrelation inherent in consecutive values across the dominant timescales.

We also exploit the idealized experiments $\widetilde{\text{EXP}}$ performed by Illig et al. (2020). They consist of 12 experiments in which downwelling EKW propagate in a seasonally varying ocean state. Idealized wind-stress perturbations are first obtained by compositing CROCO^{REF} interannual momentum fluxes for the 15 warmest Atlantic Niño events. This forcing is then used to perform CROCO simulations, such that the zonal wind-stress anomalies averaged in the Western Central Equatorial Atlantic (WCEA, [40°W–20°W; 3°S–3°N], see Figure S4a in Supporting Information S1) peak successively in each calendar month, thus forming a series of 12 experiments. For example, in $\widetilde{\text{EXP}}06$ ($\widetilde{\text{EXP}}10$), the maximum in WCEA zonal wind-stress anomalies occurs in June (October). Note that each experiment is the ensemble mean of 10 ensemble simulations. $\widetilde{\text{EXP}}$ anomalies are estimated relative to the seasonal mean-state simulated by an unperturbed experiment. In Illig et al. (2020), these experiments allowed to describe the phenology of the Atlantic Niño and Benguela Niño events and to highlight the dependence of the timing and amplitude of the events on the seasonal ocean stratification. Here, in a similar way, these simulations allow us to assess the fate of the equatorial waves along the NGG coasts, and the seasonal dependence of the amplitude and timing of the coastal variability (see Section 3.3).

2.4. Composites Associated With Strong Equatorial Wave Propagations

To characterize the coastal variability associated with strong equatorial wave propagations, we perform a composite analysis. First, we average the interannual SLA within the KATL region for CROCO^{REF} (Figure 3a)

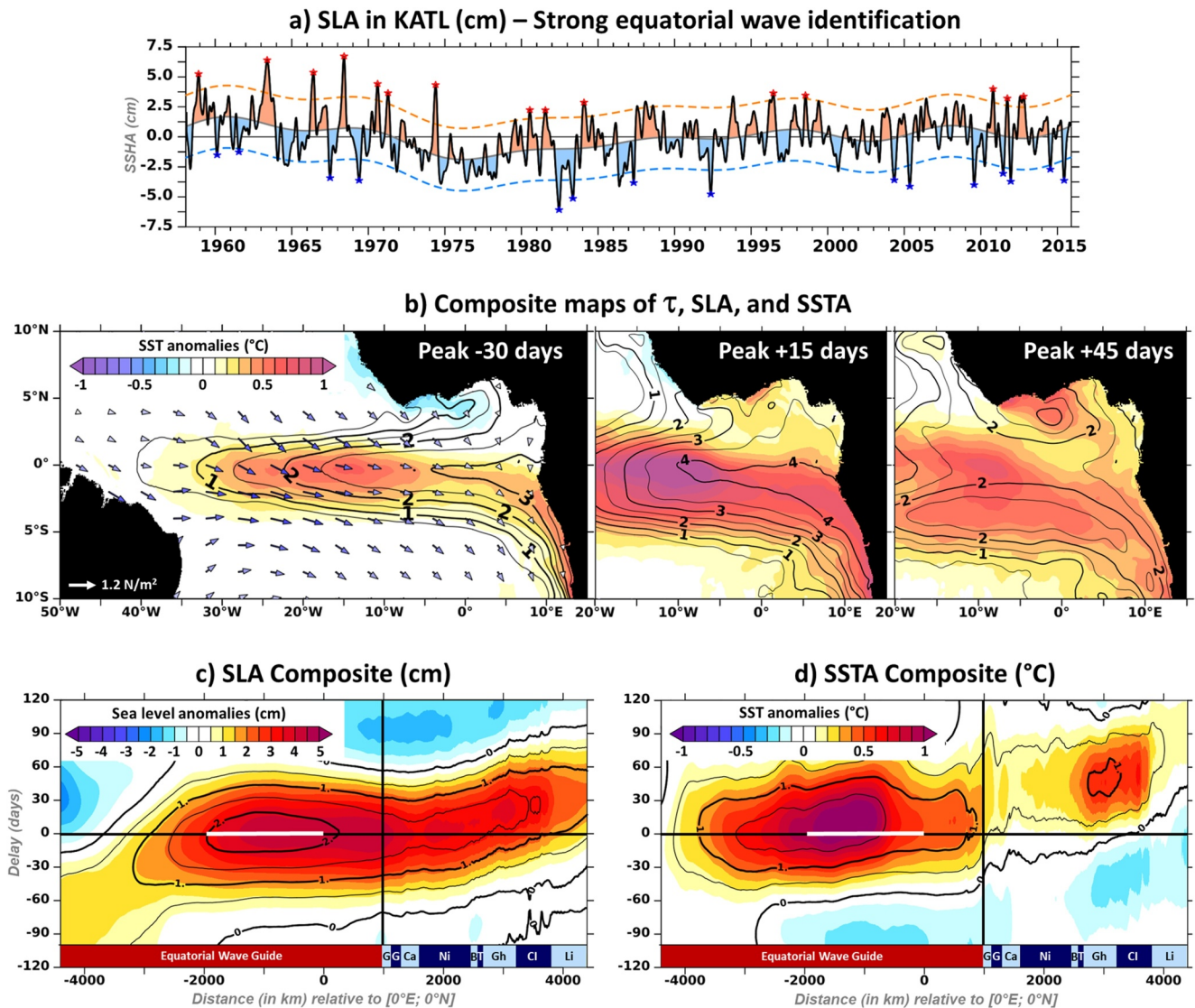


Figure 3. CROCO^{REF} composites highlighting the equatorial connection. (a) Time series of Sea Level Anomaly (SLA) (cm) averaged in the KATL box (12°W–0°E, 0.5°S–0.5°N), black line) and its decadal fluctuations (gray line). Orange and blue dashed lines show the threshold defining extreme EKW propagations (see Section 2.4), while red and blue dots highlight the peaks of the 15 downwelling (positive) and 15 upwelling (negative) energetic propagations identified. (b) Composites maps showing sea surface temperature anomaly (SSTA) (color shading, °C), SLA (contours, cm), and surface wind stress anomalies (arrows, N.m⁻²) at peak –30 days, peak +15 days, and peak +45 days. (c, d) Composite Hovmöller diagrams of SLA (cm) and SSTA (°C), respectively, as a function of the pathway of equatorial and coastal wave propagations (horizontal axis, in km) and delay relative to the KATL SLA peak (vertical axis, in days). Contours show the number of standard deviations (z-score, unitless, see Section 2.4). The white horizontal line indicates the zonal extension of the KATL domain.

and CROCO^{REMOTE} (Figure S3a in Supporting Information S1) for the period 1958–2015. The most energetic equatorial interannual propagations are identified when the KATL SLA time series exceeds 1.5 times the Standard Deviation (STD) in both CROCO^{REF} and CROCO^{REMOTE}, with peaks less than one week apart. Using this criterion, we identified 30 strong equatorial interannual propagations (15 downwelling and 15 upwelling, red and blue dots in Figure 3a and Figure S3a in Supporting Information S1). We then computed the composites for the positive (downwelling, C^+) and negative (upwelling, C^-) phases of EKWs by averaging the CROCO^{REF} temperature, temperature anomalies, SLA, and MLD at the peak of the identified events and at 3-day intervals from 120 days before to 120 days after the peak. The results revealed a high degree of symmetry between C^+ and C^- with respect to the NGG interannual coastal dynamics and thermodynamics (not shown), so that upwelling and downwelling composites can be combined together. To do this, the interannual anomalies of C^- are multiplied by -1 before averaging the two composites together. The resulting composite ($C = (C^+ - C^-)/2$) thus represents the

ocean response associated with a strong downwelling EKW propagation. To assess the strength of the composite amplitude, we calculate z -scores (standard scores) by calculating the ratio of the composite value to the standard deviation of the 58-year time series. The results are analyzed in Section 3.1.

3. Evidence of Interannual Equatorially-Forced Propagations

Using the model outputs and experiments at our disposal, we provide evidence for a strong influence of the equatorial linear dynamics on the coastal variability along the NGG coasts on interannual timescales.

3.1. Composites Analyses

We first analyze the composites of $\text{CROCO}^{\text{REF}}$ interannual anomalies associated with energetic (upwelling and downwelling) equatorial wave propagations derived from the inspection of the SLA in the eastern equatorial Atlantic (Figure 3a). Thirty extreme (15 downwelling and 15 upwelling) EKW propagations are identified (see Section 2.4). Notably, 73% of them (9 positive and 13 negative, events) peak during the May–June–July season, when the east-equatorial SLA variability is maximum (see Figure S1c in Supporting Information S1), associated with the Atlantic Niño events (Lübbecke et al., 2018). We combined the upwelling and downwelling wave signatures (see Section 2.4) and mapped the signal associated with downwelling conditions.

Figure 3b shows that these strong rises and falls in the eastern equatorial Atlantic sea level are consistent with the wind-forced linear wave dynamics (Illig et al., 2004, 2020): they are triggered by a modulation of the surface winds in the western equatorial basin and are associated with warm and cold anomalous surface conditions in the eastern equatorial Atlantic. Thirty days before the peak, the SLA composite nicely resembles an equatorially-trapped Kelvin wave, with SLAs maximum along the waveguide and confined within $[5^{\circ}\text{S}–5^{\circ}\text{N}]$. In the far eastern equatorial basin, the SLAs spread north and south, hugging the coast of Gabon, suggesting the propagation of equatorially-forced CTW. In the NGG, coastally-trapped SLAs larger than 1 cm curl up to the west, following the coastline from Nigeria to Côte d'Ivoire in a hook-shaped pattern (Figure 3b at lag -30 days), so that a local SLA minimum forms ~ 150 km off Ghana. Coastal SSTA appear few weeks later, particularly off Ghana and Côte d'Ivoire (Figure 3b at lag $+15$ and $+45$ days). We note a north-south dissymmetry, with larger coastal SLAs and SSTAs off the Angolan coast. The latter are induced by locally-forced downwelling CTW and a reduced evaporation associated with southward coastal wind anomalies connected to the remote equatorial forcing by the position and amplitude of the South Atlantic Anticyclone (Illig & Bachèlery, 2024; Illig et al., 2020). After the peak, the equatorial SLA expands on both sides of the equator (Figure 3b at lag $+15$ days), then revealing two SLA maxima on either side of the equator (Figure 3b at lag $+45$ days). These SLA maxima are located at about 4°S and 4°N , typical of the reflection of EKW into westward-propagating ERW. Due to the presence of the NGG coast near the equator, the meridional structure of the ERW is deformed and slightly asymmetric toward the equator (Cane & Sarachik, 1979; Illig et al., 2004). The northern lobe of the reflected ERW propagates close to the coast of the NGG, with a local maximum of over 3 cm in the SLAs ~ 200 km off the coast of Ghana 45 days after the peak. The SLAs are associated with SSTAs above 0.8°C along the coasts of Ghana and Côte d'Ivoire.

We further analyze the timing of the surface interannual variability along the 1° -wide equatorial and coastal waveguides (see wave path on Figure 2a). By construction, the SLA composite is maximum at lag 0 (peak phase) in the eastern equatorial Atlantic (Figure 3c) with an amplitude larger than 4 cm, exceeding 2 times the STD (see contours). Between 20°W and the coast of Gabon, the SLA maxima line up horizontally, showing no evidence of eastward propagation of the EKW. Actually, the contribution of ERW remains substantial along the equator (Illig et al., 2004, 2020) and the summed-up contribution of eastward EKW and reflected ERW wave trains results in a relatively steady pattern. In the western equatorial basin, where the EKW are forced, the sloping pattern is much slower than the theoretical phase speed of equatorial waves. It is most likely associated with the displacement of the wind-stress forcing pattern rather than the signature of free-propagating waves. In the KATL region, wave-induced temperature variations penetrate the mixed-layer and trigger SSTAs larger than 1°C , peaking ~ 10 days after the maximum in the SLA. Of particular interest is the connection between the equatorial variability and the subsequent interannual NGG variations. From Gabon to Côte d'Ivoire, coherent SLA composites of more than 3 cm, with a z -score greater than 1.5, are associated with energetic equatorial waves. With some delay, SSTAs are also detected all along the entire NGG coast (Figure 3d), but show a substantial modulation along the coastal waveguide. In agreement with Sohau et al. (2020), maximum SST fluctuations larger than 0.5°C (z -score > 1.0)

are detected off Ghana and Côte d'Ivoire, while SSTAs remain weak east of Benin and off Liberia. Furthermore, the SLA and SSTA variations along the NGG coast portray a sloping pattern with monotonically increasing lags as the distance from the KATL domain increases, especially from eastern Nigeria to western Liberia. This suggests that equatorial wave variability has a significant impact on the coastal variability in the NGG and it takes up to ~35 days (~90 days) to imprint the sea level (SST) off western Liberia. The least squares best fit to the points of maximum SLA at each position along the coastal waveguide provides an estimated phase speed of 0.8 m. s⁻¹ along Nigeria to Ghana, increasing to 1.2 m. s⁻¹ along the coasts of Côte d'Ivoire and Liberia. Notably, the SLA pattern remains fairly horizontal along the north-south oriented coasts from Gabon to Cameroon.

We now focus on the response of the coastal variability off Benin/Togo (1°E–3°E) and eastern Côte d'Ivoire (5°W–3°W) to the equatorial connection associated with energetic equatorial wave propagations (Figure 4). Off Benin-Togo (Figure 4a), the SLA (>3.5 cm; *z*-score > 1.7) peaks 12 days after the KATL SLA maximum, concomitant with a deepening of the coastal thermocline of ~10 m. The latter is associated with substantial subsurface temperature anomalies (>1.25°C; *z*-score > 1.5) in the vicinity of the thermocline (at 45 m depth), where the vertical temperature gradients are maximum. In the BT box, SSTA of less than 0.4°C (*z*-score < 0.95) lag behind the subsurface anomalies by 1 month. In the CI domain (Figure 4b), located 775 km to the west of the BT box, the SLAs take an additional 12 days to reach their maximum (>3.4 cm; *z*-score > 1.6). This underscores the propagative nature of the coastal dynamical response to the equatorial forcing, with an average phase speed of ~0.75 m. s⁻¹ between the BT and CI domains. The subsurface temperature anomalies in the CI box exhibit a tilted pattern with depth, with maximum values of 1.4°C (*z*-score = 1.4) at a significantly shallower depth (30 m) than off Benin-Togo because of the local upwelling dynamics (Djakouré et al., 2017; Philander, 1979; Varlet, 1958). In the Côte d'Ivoire upwelling system, the mean thermocline (at ~25–30 m depth) is therefore much closer to the surface mixed-layer, favoring a faster and stronger imprint on the CI SST. At lag +54 days, only 12 days after the maximum thermocline deepening (5 m), the CI SSTA exceeds 0.5°C (*z*-score > 1.0).

Figures 4c and 4d further display the equatorially-forced coastal variability as a function of the distance from the coast, allowing the examination of the cross-shore structure of the interannual surface fluctuations off Benin-Togo and Côte d'Ivoire. In both regions, the maximum in SLAs (>3.5 cm, in contours) is confined to the coast. Before lag +30 days, the SLA portrays an offshore decrease, as indicated by its negative meridional gradients, characteristic of the CTW spatial structure (Brink, 1982; Illig, Cadier, et al., 2018). Notably, the meridional extension is narrower off Côte d'Ivoire than off Benin-Togo. After lag +30 days, a dipole composed of positive meridional SLA gradients north of ~3.5°N and negative meridional gradients to the south emerges in both regions. It is characteristic of the SLA bump associated with the northern node of westward-propagating downwelling ERW waves. Because the coast of Côte d'Ivoire (at ~5.1°N) is closer to the equatorial waveguide than the coast of Benin-Togo (at ~6.3°N), the northern node of the ERW is also much closer to the coast there (Illig et al., 2004). Offshore Benin-Togo (Figure 4c), two maxima in SSTA (>0.4°C, maroon dashed contours) can be detected at lag ~+45 days, one at the coast and another located exactly where the ERW structure is maximum (~300 km offshore). Conversely, off eastern Côte d'Ivoire (Figure 4d), the SSTAs remain trapped at the coast, despite the offshore downwelling associated with the reflected ERW (~150–200 km offshore).

In both systems, within the 400 km coastal margin, the subsurface temperature anomalies actually exhibit 2 maxima located in the thermocline (Figures 4e and 4f), one at the coast and another more offshore associated with the northern node of the ERW (at ~3.5°N). The differences in the SST response between the two systems can be attributed to the different mean states in the two regions, including stratification and currents (Djakouré et al., 2017; Topé et al., 2023). Off Benin-Togo (Figure 4e), the thermocline remains relatively deep (~50 m) and flat as it approaches the coast. The deep subsurface temperature anomalies struggle to penetrate the mixed-layer and only weakly affect the coastal and offshore SST. Contrastingly, offshore Côte d'Ivoire (Figure 4f), the local upwelling dynamics (Djakouré et al., 2017; Philander, 1979; Varlet, 1958) drives coastal upward vertical currents, which raises the thermocline toward the coast. In addition, the northern maximum of the ERW and the associated subsurface temperature anomalies are ~100–150 km closer to the coast than off Benin-Togo. The modulation of the coastal upwelling associated with the passage of CTWs and ERWs thus favors a stronger imprint on the coastal margin off Côte d'Ivoire.

The result of the composite analysis revealed a strong connection between NGG coastal variability and remote equatorial forcing on interannual timescales. We showed evidence of propagating signals along the NGG coast from Nigeria to Liberia, associated with both CTW and reflected ERW propagations. Our estimate of the phase

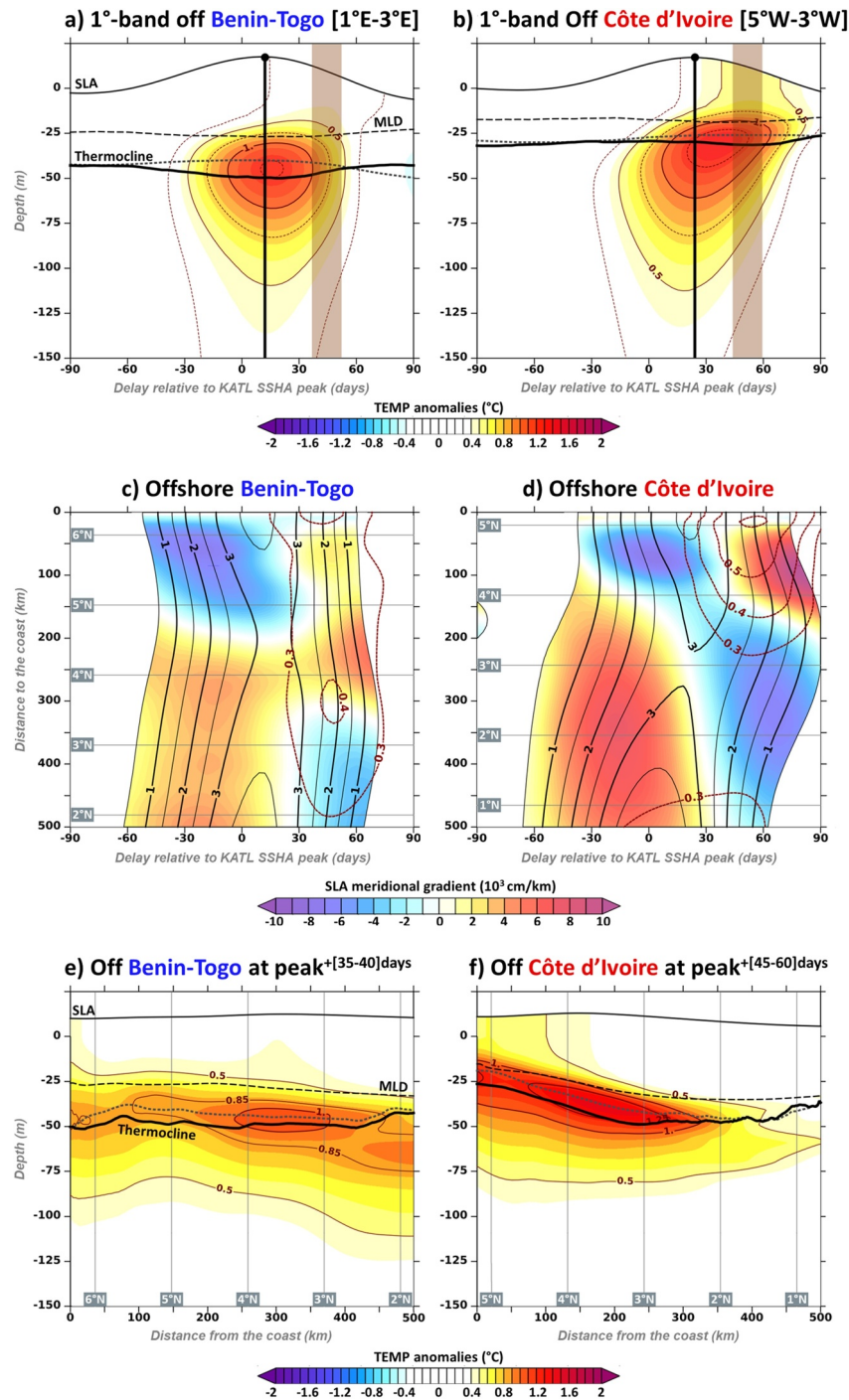


Figure 4. CROCO^{REF} composites of the coastal anomalies off Benin-Togo [1°E-3°E, left panels] and Côte d'Ivoire [5°W-3°W, right panels]. *Top panels* depict the composite of the interannual temperature anomalies (°C) averaged within the BT and CI boxes as a function of depth (m) and delay (days) to the KATL Sea Level Anomaly (SLA) peak. Exaggerated free surface variations illustrate the evolution of the SLA (SLA [in m] is multiplied by a factor of 500), with its peak marked by a vertical line. The thick line represents the position of the thermocline associated with the extreme events, while the gray dotted line indicates its climatological position. The dashed line shows the Mixed-Layer Depth. *Middle panels* show the composite of the cross-shore SLA (black contours, cm), the associated meridional gradients for SLA > 0.5 cm (colors, 10³ cm/km), and the cross-shore sea surface temperature anomaly (SSTA) (red shaded contours, °C), longitudinally averaged over the BT and CI domains as a function of the distance from the coast (km) and delay (days) to the KATL SLA peak. *Bottom panels* show the cross-shore sections as a function of depth (m) and distance from the coast (km) of the coastal anomalies, longitudinally averaged over the BT and CI domains, and over the time of maximum SSTA. For the BT (CI) domain, anomalies are averaged within [35-50] ([45-60]) days after the KATL SLA peak, as denoted by the maroon transparent rectangle in the top panels. Colors and lines are the same as in the top panels.

speed, while crude, is consistent with the theoretical phase speeds of an ERW1 of the dominant baroclinic modes (1 and 2) in the equatorial Atlantic (Illig et al., 2004). However, the theoretical phase speeds of the CTW propagating along the NGG coast are unknown. The latter vary locally depending on the coastal stratification and bathymetric slope (Brink, 1982; Illig, Cadier, et al., 2018), and only a modal decomposition of the cross-shore ocean mean state allows to infer the dominant coastal modes and their characteristics (cross-shore structure, phase speed), which is beyond the scope of the present study. In the following section, we quantify the effect of the local interannual forcing on the NGG coastal variability.

3.2. Remote Versus Local Forcing

In this section, we analyze the results of the CROCO^{REMOTE} sensitivity experiment (see Section 2.3), in which the interannual surface forcing in the eastern GoG and along the NGG coast has been filtered out, in favor of the remotely-forced coastal variability.

A swift analysis of the CROCO^{REMOTE} composites (see Figure S3 in Supporting Information S1) shows only weak differences compared to that of CROCO^{REF} (Figure 3). It confirms that when the coastal interannual forcing is removed, the north-south diverging SLA pattern associated with the poleward equatorially-forced CTW propagations (30 days before the peak) is much more symmetric toward the equator than in CROCO^{REF}. The difference between the two simulations indicates that the large-scale surface atmospheric circulation captured by the composite analysis tends to enhance the CTW signal in the south, in agreement with Illig and Bachèlery (2024) and Illig et al. (2020). Concurrently, it marginally reduces (<10%) the coastal SLA and SSTA variability in the GoG. In addition, there is a notable acceleration (10%–20%) in the phase speed of the free waves. However, the surface forcing captured by the CROCO^{REMOTE} and CROCO^{REF} composites is associated with the basin-scale response to equatorial SSTA events. The actual interannual variability of the coastal forcing is not expected to be in phase with the EKW and may be canceled-out by the compositing. In the following, we go beyond the analysis of energetic wave propagations, delving into the analysis of the interannual fluctuations over the 58 years of simulations.

We quantify the contribution of the equatorial remote forcing (as simulated by CROCO^{REMOTE}) to variability of coastal SLA (Figure 5a) and SSTA (Figure 5b) (simulated in CROCO^{REF}) along the path of equatorial and coastal wave propagations (see wave path on Figure 2a). We compute the ratio of the coastal SLA and SSTA variance between CROCO^{REMOTE} and CROCO^{REF} (shading) and the explained variance of CROCO^{REMOTE} relative to CROCO^{REF} (dashed lines). The explained variance, EXPvar, defined as:

$$\text{EXPvar} = 100 - 100 \times \left[\frac{\text{var}(\text{CROCO}^{\text{REMOTE}} - \text{CROCO}^{\text{REF}})}{\text{var}(\text{CROCO}^{\text{REF}})} \right] \quad (1)$$

quantifies the fraction of CROCO^{REMOTE} variability that is actually in phase and explains interannual fluctuations of CROCO^{REF}, as opposed to the variations caused by local surface forcing (momentum, heat and fresh water) or intrinsic nonlinearities. The results show that, over the period 1958–2015, the WCEA forcing controls to a large extent the coastal SLA variability in the NGG, leaving only a marginal role for the local forcing (Figure 5a). The variance of the CROCO^{REMOTE} coastal SLAs exceeds 70% of that of CROCO^{REF}, except in the far eastern GoG, where it drops to 60% (plain maroon line in Figure 5a). On average, the variance ratio of CROCO^{REMOTE} to CROCO^{REF} is 85% and 75% along the equator and NGG coasts, respectively. The explained variance of CROCO^{REMOTE} to CROCO^{REF} SLA is above 75% along the equator and gradually decreases along the coastal waveguide, reaching 50% off western Liberia (dashed blue line in Figure 5a). In the subsurface, the explained variance of the remotely-forced temperature anomalies in the BT and CI boxes exceeds 70% and 75%, respectively (not shown). For the SSTAs (Figure 5b), the remote equatorial forcing only partially controls the interannual variability of the NGG coast and only in regions subject to the coastal upwelling, as illustrated by the increase in the variance ratio and explained variance along the coasts of Ghana and Côte d'Ivoire. In the CI box, the variance ratio (EXPvar) reaches 40% (50%), while it remains below 25% (25%) off central Nigeria. Our results thus confirm that the local coastal dynamics modulates the surface thermal response to the remotely-forced waves along the NGG coast.

A lag correlation analysis between the SLAs in the KATL box and the SLAs within the 1°-wide path of equatorial and coastal wave propagations (Figure 5c) further underscores the control of the coastal NGG dynamics by the

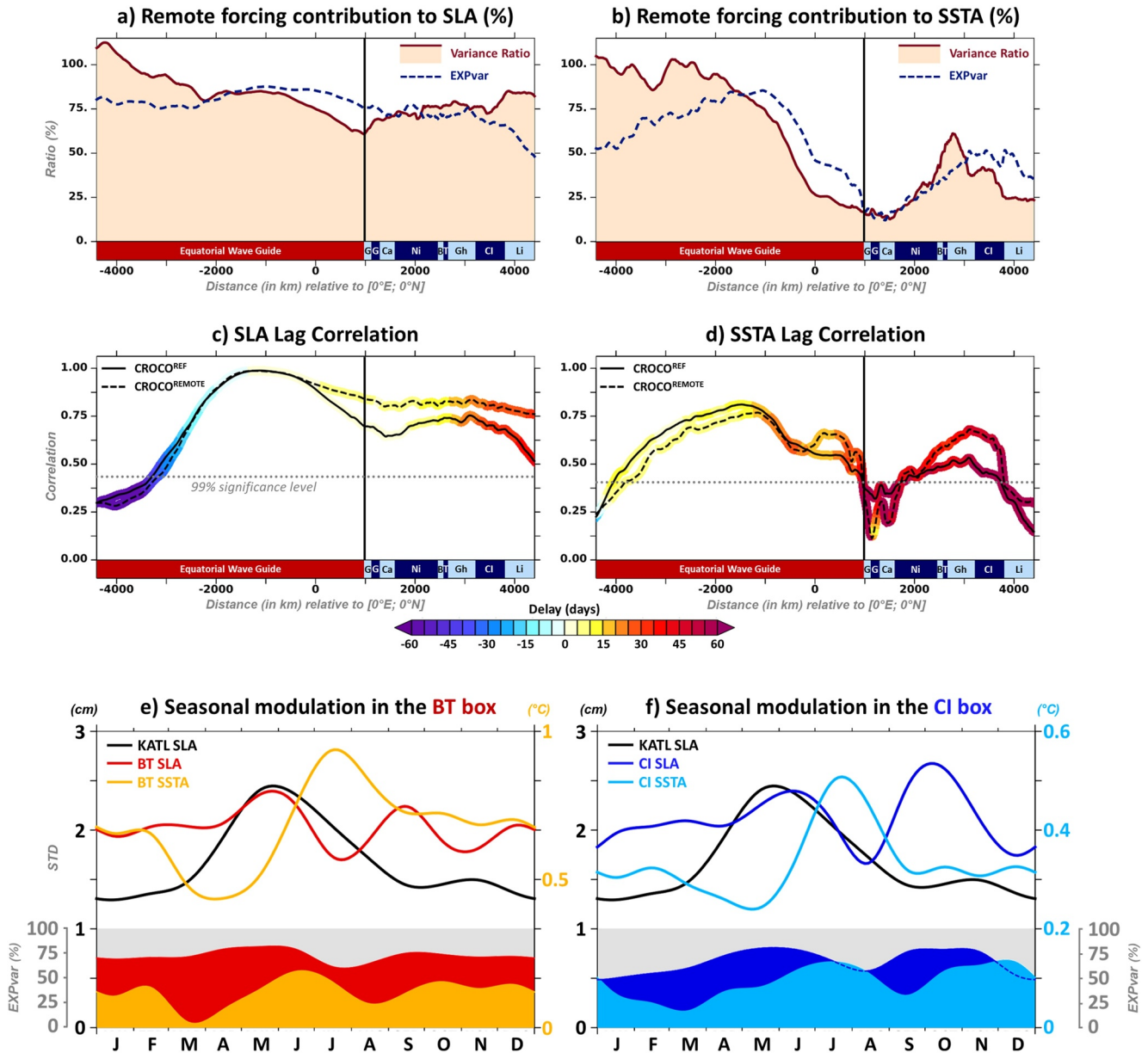


Figure 5. Equatorial remote forcing contribution to Sea Level Anomaly (SLA) (left panels) and sea surface temperature anomaly (SSTA) (right panels) along the pathway of equatorial and coastal wave propagations (x-axis, in km; see Figure 1a). *Top panels* show the ratio of variance between CROCO^{REMOTE} and CROCO^{REF} SLA (colored shading, in %) and the explained variance of CROCO^{REMOTE} with respect to CROCO^{REF} (dashed dark blue line, in %, see Equation 1). *Middle panels* show the maximum lagged correlation between the KATL SLA and the variability along the pathway of equatorial and coastal wave propagations. The plain line shows CROCO^{REF} results, while the dashed line is for CROCO^{REMOTE}. For CROCO^{REF} analysis, the lags (in days) are specified by color shading, with positive values indicating that the KATL SLA variability leads. The dotted gray line denotes the limit of the 99% significance level for the correlation. *Bottom panels* show the monthly climatology of KATL SLA STD (black line, left scale, cm) and of the coastal variability in BT (e) and CI (f) boxes. Coastal SLA STD (dark line, left scale, cm) and SSTA STD (bright line, right scale, °C). Coastal SLA and SSTA EXPvar are represented with shadings (gray scale on the side, %).

remote equatorial forcing. For CROCO^{REMOTE} (dashed line in Figure 5c), the maximum correlations ($r > 0.75$) remain largely above the threshold of statistical significance in the eastern equatorial sector and along the NGG coasts. Notably, the associated lags are monotonically increasing, confirming the propagating nature of this oceanic connection. As expected, the introduction of the interannual coastal forcing (in CROCO^{REF}) yields lower correlations (plain line in Figure 5c), yet they remain statistically significant ($r > 0.5$). The CROCO^{REF} interannual equatorial signal thus remains coherent along the entire NGG coast, with a slightly slower phase speed than for CROCO^{REMOTE}. The interannual coastal forcing does not break the link with the equatorial variability.

The analysis of the connection between the KATL SLA and the coastal SSTAs (Figure 5d) shows that the local interannual surface forcing only marginally affects the equatorial connection. Similar correlation values and lags are indeed found for $\text{CROCO}^{\text{REF}}$ and $\text{CROCO}^{\text{REMOTE}}$, showing a statistically significant connection between the equatorial variability and the SSTA fluctuations off Ghana and Côte d'Ivoire. Figures 5b and 5d thus suggest that the coastal variability is controlled to a large extent by non-linear processes. Furthermore, in contrast to the SLA analysis, the lags associated with the SSTAs are disordered, with the SSTAs off Ghana leading those off Nigeria. This again highlights the importance of local coastal dynamics and stratification, where the depth of the thermocline affects the lag and efficiency with which the remotely-forced subsurface temperature anomalies eventually imprint on the surface.

In this context, one may question whether the ocean connection with the equatorial variability on interannual timescales works for all seasons along the NGG coasts. Indeed, over the period 1958–2015, the remote equatorial forcing is more energetic in the May–June–July season, as evidenced by the seasonal STD of the KATL SLA (black line in Figures 5e and 5f), while the seasonal modulation of the coastal interannual SLA variability also exhibits a secondary peak later in the year (August–September–October) in both the BT (dark red line in Figure 5e) and CI (dark blue line in Figure 5f) boxes. The results show that the equatorial forcing remains detrimental to explaining the coastal SLA variations in both seasons, as illustrated by the seasonal modulation of EXPvar. Notably, the coastal interannual SSTA variability has most of its variability concentrated in one season during June–July–August (orange line in Figure 5e for the BT box and light blue line in Figure 5f for the CI box). Nevertheless, the connection with the equatorial variability remains important in the two seasons characterized by high coastal SLA variability. As a result, the surface response is not linear with respect to the equatorial forcing.

Our results show that the connection with the equatorial variability is detrimental to explaining the coastal variability, but there is a substantial seasonal modulation that must be taken into account when analyzing the timing and amplitude of the surface variability. In the following section, we further analyze this seasonal modulation, focusing on the role of the seasonally-varying conditions along the NGG coast.

3.3. Effect of the Seasonal Cycle of the Coastal Stratification

In this section, we analyze the results of idealized model experiments ($\widetilde{\text{EXP}}$, see Section 2.3) in which a wind-stress perturbation, applied sequentially in each month of the year, triggers a downwelling EKW in the WCEA (and subsequent ERW and CTW) that propagates over a seasonally-varying ocean mean state. These experiments were used in Illig et al. (2020) to document the interannual variability in the eastern equatorial region and along the West African coast off Angola-Namibia. Here, we apply their methodology and diagnostics to further investigate the timing and seasonal modulation of the remote equatorial variability in the NGG and to compare the dynamics along the coasts of Benin-Togo and Côte d'Ivoire.

The top panels of Figure 6 show the $\widetilde{\text{EXP}}$ ensemble-mean surface dynamical (SLA, Figure 6a) and thermodynamic (SSTA, Figure 6b) responses in the BT box over a 9-month period (horizontal axis) to identical wind-stress anomalies prescribed during different seasons (vertical axis). The blue vertical dashed line indicates when the zonal wind-stress anomaly is maximum in the WCEA (Figure S4a in Supporting Information S1), with the corresponding month indicated on the vertical axis label. The black rectangles in Figure 6b indicate the month of July for each experiment. The results show that, on average over the 12 experiments, the BT SLA variability lags the KATL SLA fluctuations by 11 days, which is in good agreement with the composite analysis (see Section 3.1 and Figures 3a and 3b). Notably, we detect a substantial seasonal modulation of the amplitude and timing of the maximum downwelling anomalies of the SLA, with maximum values (>3 cm) and larger lags noted when the forcing is applied in the March–April–May season and during the second half of the year. This pattern is similar to that reported in the eastern equatorial Atlantic and off Angola-Namibia (see Figures 8 and 9 in Illig et al. (2020) and Figure S4b in Supporting Information S1). It can be related to the seasonal maximum of the second mode wind-stress projection coefficient (see Figure A2 in Illig et al. (2004)). Consistent with the composites analysis (see Section 3.1), the surface warming in the BT box remains weak, mostly below 0.4°C .

The maximum SSTA ($>0.3^\circ\text{C}$) occurs when the remote forcing is applied during the April–May–June season (Figure 6b), and in this season it lags the BT SLA by ~ 3 –4 weeks. $\widetilde{\text{EXP06}}$ (plain maroon rectangle in Figure 6b) experiences the largest SSTA in the BT box, with a peak of 0.43°C during the month of July, in agreement with

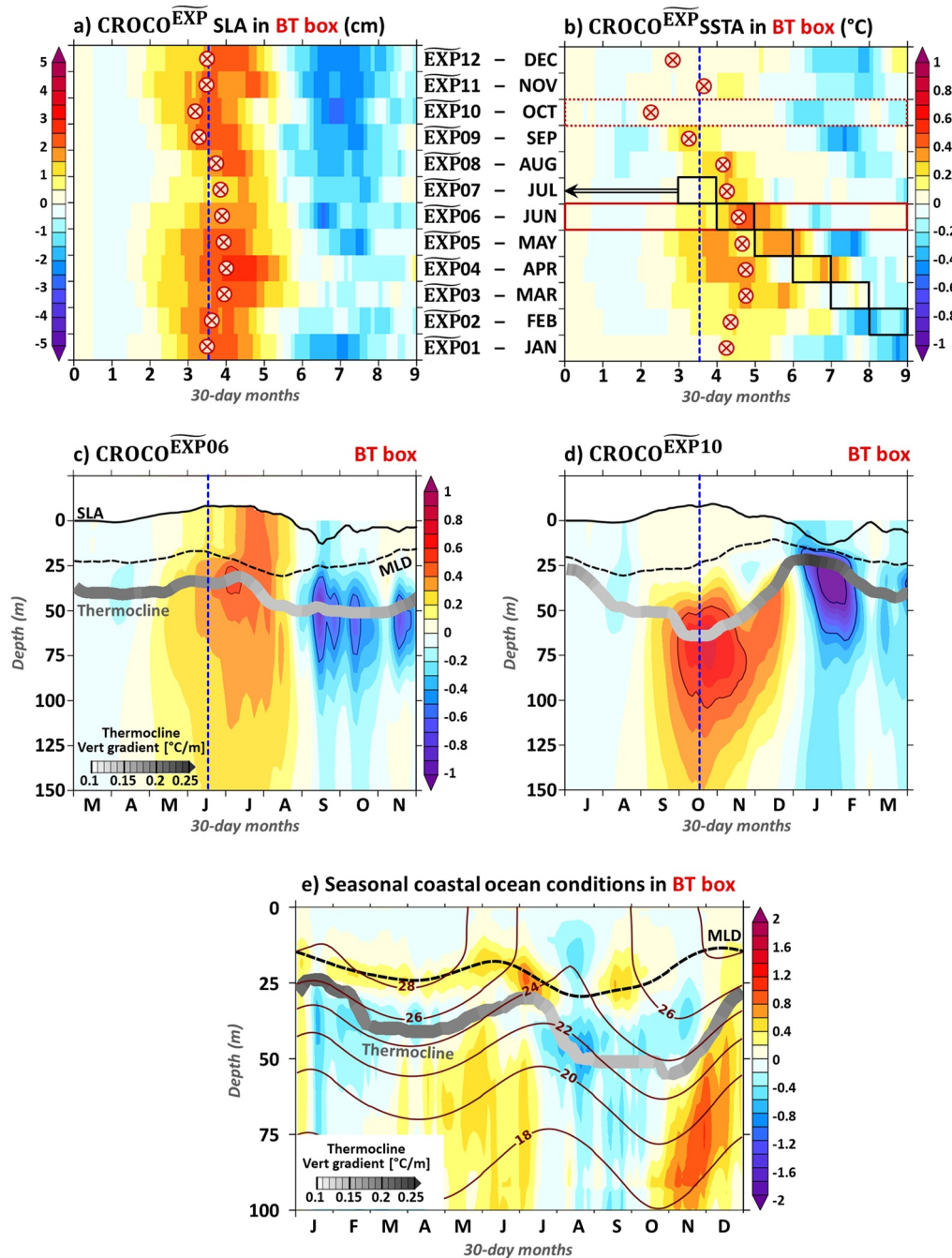


Figure 6. Influence of seasonal stratification in the Benin-Togo coastal domain (BT). *Top panels* show $\overline{\text{EXP}}$ ensemble-mean Sea Level Anomaly (SLA) (a, in cm) and sea surface temperature anomaly (SSTA) (b, in °C) averaged over the BT box, plotted against time (horizontal axis, in months) across the 12 idealized experiments (vertical axis). The circled crosses indicate the lag at which the correlation between Western Central Equatorial Atlantic (WCEA) zonal wind-stress perturbations and CROCO-EXP BT SLA is maximized, arbitrarily positioned relative to the peak in WCEA zonal wind-stress perturbations (see Figure S4a in Supporting Information S1), indicated by the blue vertical dashed line. In panel (b), black rectangles highlight the month of July in each EXP experiment. *Middle panels* show the ensemble-mean of the CROCO-EXP06 (c) and CROCO-EXP10 (d) anomalies, averaged over the BT box. Color shading represents the temperature anomalies (in °C) relative to the unperturbed EXP ensemble-mean as a function of depth (in m) and time. Exaggerated free surface variations illustrate the evolution of the Sea Level Anomaly (SLA) (SLA [in m] is multiplied by a factor of 500). The black dashed line shows the Mixed-Layer Depth (MLD). The polytube shows the depth of the thermocline, with gray shading quantifying the associated vertical temperature gradients (°C/m). The blue vertical dashed line indicates when the WCEA zonal wind-stress anomalies are strongest. The *bottom panel* shows the seasonal ocean conditions in the BT box from the unperturbed EXP ensemble mean, with vertical velocity (color shading, m/day), temperature (contours, °C), thermocline depth and associated vertical gradients (polytube, °C/m), and the MLD (dashed line).

the seasonal maximum of BT SSTA interannual variability (Figure 5e). The associated subsurface warming reaches 0.56°C in mid-June (Figure 6c) at 30 m-depth, where the vertical thermal gradients are maximum (gray-shaded ribbon). At this time of year, the thermocline is quite shallow (25–30 m) and close to the base of the mixed-layer (Figure 6e). In July, the thermocline although slightly deepened by the downwelling wave (~ 5 m), is less than 10 m below the base of the mixed-layer (Figure 6b). In addition, there is an intensification of the vertical upwelling at the base of the mixed-layer in July (Figure 6e), locally induced by the vertical divergence caused by the Guinea undercurrent hitting the coast. The mean ocean conditions in July thus provide a very effective subsurface/surface coupling which leads to the strongest SSTA signature in $\widetilde{\text{EXP06}}$ (Figure 6b).

Conversely, when the WCEA wind-stress anomaly is prescribed in October–January, the surface warming is very weak ($<0.2^{\circ}\text{C}$, see Figure 6b). In the BT box, the minimum SSTA response is recorded for $\widetilde{\text{EXP10}}$ (dashed maroon rectangle in Figure 6b), with positive SSTA not exceeding 0.1°C . The month of October corresponds to the season associated with the deepest thermocline along the Benin-Togo coast (>55 m deep, Figure 6e), but is also associated with the lowest vertical thermal gradients. The wave-induced deepening of the thermocline is therefore more important (>13 m). As a result, the subsurface warming ($\sim 0.78^{\circ}\text{C}$ at 68 m-depth), although more intense than in $\widetilde{\text{EXP06}}$ (by a factor of 1.4), is more than 40 m deeper than the base of the mixed-layer and does not imprint the SST. The ratio between the maximum and minimum thickness of the layer separating the thermocline and the base of the mixed-layer is ~ 4 , as is the seasonal modulation of the SSTA in the BT box. Notably, the BT SSTA interannual variability is minimum in March–April–May (Figure 5f), when the thermocline is also quite deep. However, it does not coincide with the $\widetilde{\text{EXP}}$ seasonal minimum of the remotely-forced SSTA, suggesting that coastal surface forcing or nonlinear dynamics may be an additional source of SST variability during this season.

Furthermore, the SSTA response in the first 100 km off the Benin-Togo coast (Figure 6b) is quite different from that reported in the eastern equatorial Atlantic or in the coastal Angola Benguela area (see Figures 8 and 9 in Illig et al. (2020) and Figure S4bc in Supporting Information S1). In fact, the BT SSTA response often exhibits 2 maxima, while the subsurface anomalies always portray only one core of maximum warming. The maxima in the SSTA either classically lag behind the equatorial forcing by a few weeks ($\widetilde{\text{EXP01-05}}$), or they are drawn to the July–August season (see the diagonal alignment in $\widetilde{\text{EXP04-09}}$), when the ocean mean state is most favorable for the penetration of subsurface anomalies into the surface layer (Figure 6e). The amplitude and timing of the surface temperature anomalies are thus dictated by the mean state of the coastal ocean (stratification, currents), which makes it difficult to anticipate the delay of the SST response to the equatorial wave forcing.

Along the coast of Côte d'Ivoire (Figure 7) and on average over the 12 experiments, the SLA variability lags the KATL (BT) SLA fluctuations by 26 (12.5) days. It takes another month for the subsurface warming to imprint on the SST, which is in good agreement with the composite analysis (see Section 3.1 and Figures 4a and 4b). The CI SLAs also exhibit a seasonal modulation of their amplitude and timing (Figure 7a), consistent with the equatorial forcing (Figure S4b in Supporting Information S1). The SSTA response in the CI box is much larger than along the Benin-Togo coast (Figure 7b), with maximum surface warming ($>0.7^{\circ}\text{C}$) when the remote forcing is applied during the April–August season, the major upwelling season (Arfi et al., 1991; Morlière, 1970, see Figure 1c). In $\widetilde{\text{EXP06}}$ (plain maroon rectangle in Figure 7b), the SSTA averaged in the CI box exceeds 0.8°C . In contrast to the BT region, the associated subsurface anomalies (Figure 7c) are composed of two distinct maxima, one in July and another more intense in August. Both cores are located in the vicinity of the thermocline, which is relatively shallow in this season (<20 m depth, Figures 7c and 7e) and almost brush against the mixed-layer (distance is less than 5 m) due to the upwelling dynamics. The seasonal upwelling favors the penetration of the subsurface anomalies into the mixed-layer and the surface warming peaks in August.

Contrastingly, the SSTA response in the CI box is weak when the WCEA wind-stress anomaly is prescribed in October–December (Figure 7b). The minimum SSTA response is recorded for $\widetilde{\text{EXP11}}$ (dashed maroon rectangle in Figure 7b). However, it is associated with intense remotely-forced subsurface warming ($>1^{\circ}\text{C}$ at 48 m depth, Figure 7d). As in $\widetilde{\text{EXP06}}$, the subsurface anomalies in $\widetilde{\text{EXP11}}$ are composed of two maxima within 1 month of each other (in late November and December). Analysis of the mean ocean conditions in the CI box (Figure 7e) reveals that the November–December season does not favor the surface/subsurface coupling. It is indeed associated with the deepest thermocline (>40 m deep) and the thinnest mixed-layer (<10 m deep). Despite the

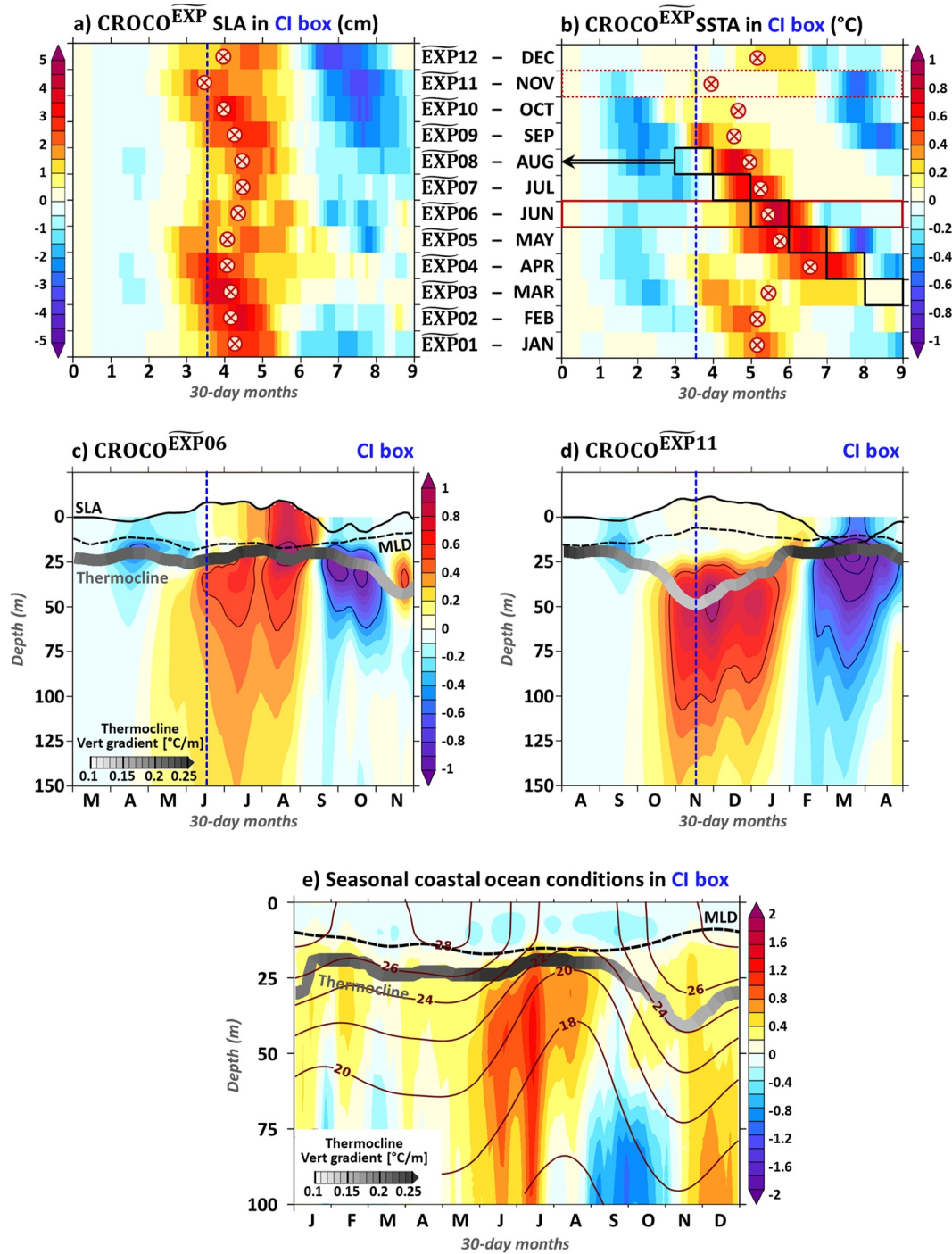


Figure 7. Same as Figure 5, but for the Côte d'Ivoire coastal domain (CI). Black rectangles in panel (c) show the month of August associated with each $\widetilde{\text{EXP}}$ experiments. The results of $\widetilde{\text{EXP}}$ 11 are presented in panel (d).

moderate upwelling conditions in November–December, the subsurface warming does not propagate to the surface mixed-layer.

Notably, during the minor upwelling season (Arfi et al., 1991; Morlière, 1970, see Figure 1a) in February–March, the mean thermocline is once again close to the base of the mixed-layer and associated with an upward vertical current (Figure 7e), favoring the surface wave-induced signature on the SST. As a result, the

SSTA response to the remote forcing (Figure 7b) portrays a pattern composed of two diagonals, with maximum surface warmings drawn to the two upwelling seasons (in July–August–September and February–March–April), to the extent that in EXP02–04 the surface warming is split in two. This ultimate control of the surface thermal response by the coastal stratification and circulation conditions breaks any consistency in the analysis of the delay relative to the dynamical signature associated with the waves, as shown by the jumbled lags estimates in Figure 7b.

4. Summary, Discussion, and Conclusions

In this paper, we documented the ocean connection between linear equatorial dynamics and coastal variability along the northern coast of the GoG on interannual timescales. Our approach is based on numerical experiments with a high-resolution ocean model of the Tropical Atlantic for the period 1958–2015, applying the methods used to study the coastal interannual variability in the Angola-Benguela upwelling system (Bachèlery et al., 2016a, 2020; Illig et al., 2020). Composite analyses associated with energetic interannual EKWs, generated by wind-stress anomalies in the west-central equatorial basin, revealed a strong signature on the NGG coastal sea level. The remotely-forced coastal SLAs are greater than 3 cm and exhibit a clear poleward propagative nature from the coasts of Cameroon, Nigeria, Benin, Togo, Ghana, Côte d'Ivoire, to Liberia. This propagation, which is associated with coastal SST variations of 0.5–1°C, takes about 1.5 months to reach the coast of Sierra Leone, corresponding to a phase speed of 0.75–1.2 m.s^{−1}. On the investigation of remote versus local forcing, a sensitivity experiment in which the interannual surface forcing along the NGG coast was removed showed that the remote equatorial forcing significantly controls the coastal SLAs (up to 70%–80%), especially in the boreal spring and fall, leaving only a marginal role for the local atmospheric forcing (momentum, heat, and fresh-water fluxes). However, we reported that the surface forcing in the eastern GoG and along the NGG coast tends to accelerate the coastal propagations by 10%–20% of its phase-speed.

Furthermore, our results show that the remotely-forced interannual coastal SLAs reflect strong subsurface temperature anomalies in the vicinity of the thermocline and a substantial modulation of the thermocline depth along the entire NGG coast. However, the remote equatorial forcing explains more of the SSTA variance for the coastal systems associated with clear upwelling characteristics such as Côte d'Ivoire and Ghana, in agreement with Sohau et al. (2020). The coastal upwelling dynamics yields a rise of the thermocline toward the coast, bringing it closer to the base of the mixed-layer and favoring an effective subsurface/surface coupling. In this context, a drastic seasonal modulation of the surface thermal response is further diagnosed off Côte d'Ivoire and Benin-Togo, associated with the seasonal variations of the coastal stratification and circulation (Djakouré et al., 2017; Topé et al., 2023). As a result, there is a weak consistency in the delay at which the SSTAs peak relative to the dynamical signature associated with the waves (extremum in SLAs, thermocline depth variations, or subsurface temperature anomalies). Therefore, SST is not a suitable variable for tracking coastal propagations in the GoG, as illustrated in Figure 2c. In fact, along their propagation, the coastal waves encounter different ecosystems, characterized by different mean conditions and seasonal cycles, in which the subsurface anomalies take different times to imprint on the mixed-layer.

Additionally, due to the proximity of the NGG coastline to the equator, the coastal variability appears to be influenced by both CTWs and ERWs. Poleward-propagating CTW are excited by incoming EKW forced in the west-central equatorial basin, propagating westward from Cameroon to Sierra-Leone. The westward-propagating ERWs result from the reflection of the incident EKW at the eastern boundary of the equatorial basin, with their northern node located at 3–4°N. The ERWs are notably close to the coast of Côte d'Ivoire, situated at ~5°N. In this region, we have in fact detected multiple maxima of subsurface temperature anomalies associated with remotely-forced coastal variability (Figures 7c and 7d), contrasting with the 100 km-wide coastal fringe off Benin-Togo, where such structures were not reported. These anomalies may be associated with these different types of waves or may indicate the signature of different vertical modes. Wave modes, characterized by specific phase speeds can indeed separate during their propagation. Only by decomposing the cross-shore variability into dominant CTW (Illig, Bachèlery, & Cadier, 2018; Illig, Cadier, et al., 2018) and ERW (Illig et al., 2004) modes can we untangle the effects of each wave type, gaining a deeper understanding of the coastal structure and timing of the coastal response to the equatorial forcing. Furthermore, our results call for complementary analyses based on the Tropical Atlantic observational network (Foltz et al., 2019). PIRATA data (Prediction and Research Moored Array in the Tropical Atlantic, Bourlès et al., 2019) can be used to monitor the equatorial wave activity (as in Imbol Koungue

et al., 2017), and onset temperature measurements (Sohou et al., 2020), together with the upcoming Surface Water Ocean Topography (Morrow et al., 2019) high-resolution sea level observations can provide surface coastal conditions.

The coastal region off NGG has historically received less attention with respect to the impact of remote equatorial variability on interannual timescales, in comparison to well-studied upwelling systems such as the Angola-Benguela upwelling system. However, this first comprehensive study presents compelling evidence for a robust oceanic connection, revealing significant remotely-forced subsurface temperature anomalies, thermocline movements, and SLAs along the NGG coasts. The magnitude and propagating speed of these interannual anomalies are comparable to those documented off the coasts of Angola and Namibia, as reported by Bachèlery et al. (2016a, 2020). In contrast to the coastal band off southwest Africa, the diversity of ecosystems along the NGG coastline yields a strong modulation of the amplitude and timing of the equatorially-forced SSTA variability. The strongest fluctuations are detected in the Côte d'Ivoire/Ghana upwelling system, whose SSTA variations rival those of the Angola-Benguela system. Similar to the biogeochemical dynamics in the Angola-Benguela upwelling system (Bachèlery et al., 2016b), the wave-associated vertical currents off Côte d'Ivoire and Ghana can also modulate the nutrient intake into the sunlit layer, affecting primary production and fish habitat. Remarkably, due to the propagative nature of this oceanic connection associated with long wave propagations forced remotely in the western equatorial basin, our findings open the possibility of predicting interannual changes in coastal conditions off NGG a few months in advance. This predictive capability holds the key to anticipating the impacts on pelagic fish habitats and resources, thereby enabling proactive measures for sustainable management and conservation efforts in this upwelling system.

Acronyms

BT	Benin-Togo coastal domain [1°E–3°E; 1°-wide coastal margin]
CARS2009	2009 CSIRO Atlas of Regional Seas climatology
CI	Côte d'Ivoire coastal domain [5°W–3°W; 1°-wide coastal margin]
CROCO	Coastal and Regional Ocean COMMunity model
CTWs	Coastal Trapped Waves
EKW	Equatorial Kelvin Wave
ERW	Equatorial Rossby Wave
GoG	Gulf of Guinea
KATL	Equatorially-trapped Kelvin wave domain [20°W–0°E; 0.5°S–0.5°N]
MLD	Mixed-Layer Depth
NGG	North of the Gulf of Guinea
SLA	interannual Sea Level Anomaly
SST	Sea Surface Temperature
SSTA	interannual Sea Surface Temperature Anomaly
STD	STandard Deviation
WCEA	Western-Central Equatorial Atlantic

Conflict of Interest

The authors declare no conflicts of interest relevant to this study.

Data Availability Statement

Remote-sensed observations (Figure 1) and CROCO model outputs (Figures 2–6) used in this study have been archived for public access in Illig (2024). The CROCO and CROCO_Tools software can be downloaded from the CROCO website (<https://www.croco-ocean.org>). PyFerret, developed by NOAA's Pacific Marine Environmental Laboratory, is available at <http://ferret.pmel.noaa.gov/Ferret>. Additionally, AVISO altimetric data, NOAA Optimum Interpolation SST, GEBCO topography, DRAKKAR Forcing fields, and CARS2009 monthly climatology are freely accessible to the public on their respective program websites.

Acknowledgments

We thank Dr. P. Marchesiello (LEGOS) for fruitful discussions on ocean dynamics. Model simulations were conducted on the CALMIP supercomputer at the University of Toulouse (France) under the CALMIP project 19002. The CROCO model grid, forcing, and initial conditions were generated using the CROCO_Tools software (Penven et al., 2007). The authors would like to acknowledge the use of the PyFerret program for data analyses and graphical representations in this paper. Sandrine Djakouré has received funding from TRIATLAS and the French National Research Institute for Sustainable Development (IRD, JEAI IVOARE-UP project). Toussaint Mitchodigni was supported by the ERASMUS+ program during his scientific mission at LEGOS (Toulouse, France).

References

- Ali, K., Kouadio, K., Zahiri, G., Aman, A., Assamoi, A., & Bourlès, B. (2011). Influence of the Gulf of Guinea coastal and equatorial upwellings on the precipitations along its northern coasts during the boreal summer period. *Asian Journal of Applied Sciences*, 4(3), 271–285. <https://doi.org/10.3923/ajaps.2011.271.285>
- Alory, G., Da-Allada, C. Y., Djakouré, S., Dadou, I., Jouanno, J., & Loemba, D. P. (2021). Coastal upwelling limitation by onshore geostrophic flow in the Gulf of Guinea around the Niger River Plume. *Frontiers in Marine Science*, 7, 607216. <https://doi.org/10.3389/fmars.2020.607216>
- Amemou, H., Koné, V., Aman, A., & Lett, C. (2020). Assessment of a Lagrangian model using trajectories of oceanographic drifters and fishing devices in the Tropical Atlantic Ocean. *Progress in Oceanography*, 188, 102426. <https://doi.org/10.1016/j.pocan.2020.102426>
- Arfi, R., Pezennec, O., Cissoko, S., & Mensah, M. (1991). Variations spatiale et temporelle de la résurgence ivoiro-ghanéenne. In P. Cury & C. Roy (Eds.), *Pêcheries ouest-africaines. Variabilité, instabilité et changement* (pp. 162–172). Orstom.
- Auclair, F., Benshila, R., Bordoïs, L., Boutet, M., Brémond, M., Caillaud, M., et al. (2022). Coastal and Regional Ocean Community model (1.3). *Zenodo*. <https://doi.org/10.5281/zenodo.7415343>
- Bachèlery, M. L., Illig, S., & Dadou, I. (2016a). Interannual variability in the South-East Atlantic Ocean, focusing on the Benguela Upwelling System: Remote versus local forcing. *Journal of Geophysical Research: Oceans*, 121(1), 284–310. <https://doi.org/10.1002/2015JC011168>
- Bachèlery, M.-L., Illig, S., & Dadou, I. (2016b). Forcings of nutrient, oxygen and primary production interannual variability in the South-East Atlantic Ocean. *Geophysical Research Letters*, 43(16), 8617–8625. <https://doi.org/10.1002/2016GL070288>
- Bachèlery, M. L., Illig, S., & Rouault, M. (2020). Interannual coastal trapped waves in the Angola-Benguela upwelling system and Benguela Niño and Niña events. *Journal of Marine Systems*, 203(March 2020), 103262. <https://doi.org/10.1016/j.jmarsys.2019.103262>
- Binet, D., & Marchal, E. (1993). The large marine ecosystem of shelf areas in the Gulf of Guinea: Long-term variability induced by climatic changes. In K. Sherman, L. M. Alexander, & B. D. Gold (Eds.), *Large marine ecosystems: Stocks, mitigation and sustainability* (pp. 104–118). AAAS Publication 92-395.
- Binet, D., & Servain, J. (1993). Have the recent hydrological changes in the Northern Gulf of Guinea induced the *Sardinella aurita* outburst. *Oceanologica Acta*, 16(3), 247–260.
- Bourlès, B., Araujo, M., McPhaden, M. J., Brandt, P., Foltz, G. R., Lumpkin, R., et al. (2019). PIRATA: A sustained observing system for tropical Atlantic climate research and forecasting. *Earth and Space Science*, 6(4), 577–616. <https://doi.org/10.1029/2018EA000428>
- Brandt, P., Alory, G., Awo, F. M., Dengler, M., Djakouré, S., Imbol Koungue, R. A., et al. (2023). Physical processes and biological productivity in the upwelling regions of the tropical Atlantic. *Ocean Science*, 19(3), 581–601. <https://doi.org/10.5194/os-19-581-2023>
- Brandt, P., Caniaux, G., Bourlès, B., Lazar, A., Dengler, M., Funk, A., et al. (2011). Equatorial upper-ocean dynamics and their interaction with the West African monsoon. *Atmospheric Science Letters*, 12(1), 24–30. <https://doi.org/10.1002/asl.287>
- Brink, K. H. (1982). A comparison of long Coastal Trapped Wave theory with observations off Peru. *Journal of Physical Oceanography*, 12(8), 897–913. [https://doi.org/10.1175/1520-0485\(1982\)012<0897:acolct>2.0.co;2](https://doi.org/10.1175/1520-0485(1982)012<0897:acolct>2.0.co;2)
- Burles, N. J., Reason, C. J. C., Penven, P., & Philander, S. G. (2011). Similarities between the tropical Atlantic seasonal cycle and ENSO: An energetics perspective. *Journal of Geophysical Research*, 116(C11), C11010. <https://doi.org/10.1029/2011jc007164>
- Burmeister, K., Lübbecke, J. F., & Brandt, P. (2016). Revisiting the cause of the eastern equatorial Atlantic cold event in 2009. *Journal of Geophysical Research: Ocean*, 7, 4777–4789. <https://doi.org/10.1002/2016JC011719>
- Cane, M. A., & Sarachik, E. S. (1979). Forced baroclinic ocean motions. III: The linear equatorial basin case. *Journal of Marine Research*, 37, 355–398.
- Caniaux, G., Giordani, H., Redelsperger, J. L., Guichard, F., Key, E., & Wade, M. (2011). Coupling between the Atlantic cold tongue and the West African monsoon in boreal spring and summer. *Journal of Geophysical Research*, 116(C4), C04003. <https://doi.org/10.1029/2010jc006570>
- Carton, J., & Huang, B. (1994). Warm events in the tropical Atlantic. *Journal of Physical Oceanography*, 24(5), 888–903. [https://doi.org/10.1175/1520-0485\(1994\)024<0888:WEITTA>2.0.CO;2](https://doi.org/10.1175/1520-0485(1994)024<0888:WEITTA>2.0.CO;2)
- Clarke, A. J. (1983). The reflection of equatorial waves from oceanic boundaries. *Journal of Physical Oceanography*, 13(7), 1193–1207. [https://doi.org/10.1175/1520-0485\(1983\)013<1193:troewf>2.0.co;2](https://doi.org/10.1175/1520-0485(1983)013<1193:troewf>2.0.co;2)
- Clarke, A. J., & Battisti, D. S. (1983). Identification of the fortnightly wave observed along the northern coast of the Gulf of Guinea. *Journal of Physical Oceanography*, 13(12), 2192–2200. [https://doi.org/10.1175/1520-0485\(1983\)013<2192:IOTFWO>2.0.CO;2](https://doi.org/10.1175/1520-0485(1983)013<2192:IOTFWO>2.0.CO;2)
- Clarke, A. J., & Brink, K. H. (1985). The response of stratified, frictional flow of shelf and slope waters to fluctuating largescale low-frequency wind forcing. *Journal of Physical Oceanography*, 15(4), 439–453. [https://doi.org/10.1175/1520-0485\(1985\)015<0439:trosff>2.0.co;2](https://doi.org/10.1175/1520-0485(1985)015<0439:trosff>2.0.co;2)
- Da-Allada, C. Y., Agada, J., Baloticha, E., Houkonnou, M. N., Jouanno, J., & Alory, G. (2021). Causes of the Northern Gulf of Guinea Cold Event in 2012. *Journal of Geophysical Research: Oceans*, 126(8), e2021JC017627. <https://doi.org/10.1029/2021JC017627>
- Debreu, L., Marchesiello, P., Penven, P., & Cambon, G. (2012). Two-way nesting in split-explicit ocean models: Algorithms, implementation and validation. *Ocean Modelling*, 49–50, 1–21. <https://doi.org/10.1016/j.ocemod.2012.03.003>
- de Coëtlogon, G., Deroubaix, A., Flamant, C., Menut, L., & Gaetani, M. (2023). Impact of the Guinea coast upwelling on atmospheric dynamics, precipitation and pollutant transport over southern West Africa. *Atmospheric Chemistry and Physics*, 23(24), 15507–15521. <https://doi.org/10.5194/acp-23-15507-2023>
- Ding, H., Keenlyside, N. S., & Latif, M. (2009). Seasonal cycle in the upper equatorial Atlantic Ocean. *Journal of Geophysical Research*, 114(C9), C09016. <https://doi.org/10.1029/2009jc005418>
- Djakouré, S., Penven, P., Bourlès, B., Koné, V., & Veitch, J. (2017). Respective roles of the Guinea Current and local winds on the coastal upwelling in the Northern Gulf of Guinea. *Journal of Physical Oceanography*, 47(6), 1367–1387. <https://doi.org/10.1175/JPO-D-16-0126.1>

- Djakouré, S., Penven, P., Bourlès, B., Veitch, J., & Kone, V. (2014). Coastally trapped eddies in the north of the Gulf of Guinea. *Journal of Geophysical Research: Oceans*, 119(10), 6805–6819. <https://doi.org/10.1002/2014jc010243>
- Dunn, J. (2009). *CARS 2009: CSIRO Atlas of regional seas*. Mar.Lab.,Commonw. Sci. and Ind.Res. Organ. Retrieved from <http://www.marine.csiro.au/~dunn/cars2009/>
- Dussin, R., Barnier, B., & Brodeau, L. (2016). *The making of Drakkar forcing set DFS5*. DRAKKAR/MyOcean Rep. 01–04-16. Laboratoire de Glaciologie et Géophysique de l'Environnement.
- Foltz, G. R., Brandt, P., Richter, I., Rodriguez-Fonsecao, B., Hernandez, F., Dengler, M., et al. (2019). The Tropical Atlantic Observing System. *Frontiers in Marine Science*, 6, 206. <https://doi.org/10.3389/fmars.2019.00206>
- Foltz, G. R., & McPhaden, M. J. (2010). Interaction between the Atlantic meridional and Niño modes. *Geophysical Research Letters*, 37(18), L18604. <https://doi.org/10.1029/2010GL044001>
- Fontaine, B., & Janicot, S. (1992). Wind-field coherence and its variations over West Africa. *Journal of Climate*, 5, 512–524. [https://doi.org/10.1175/1520-0442\(1992\)005<0512:wfaiv>2.0.co;2](https://doi.org/10.1175/1520-0442(1992)005<0512:wfaiv>2.0.co;2)
- Hardman-Mountford, N. J., & McGlade, J. M. (2003). Seasonal and interannual variability of oceanographic processes in the Gulf of Guinea: An investigation using AVHRR sea surface temperature data. *International Journal of Remote Sensing*, 24(16), 3247–3268. <https://doi.org/10.1080/0143116021000021297>
- Huang, B., Liu, C., Banzon, V., Freeman, E., Graham, G., Hankins, B., et al. (2021). Improvements of the Daily Optimum Interpolation Sea Surface Temperature (DOISST) version 2.1. *Journal of Climate*, 34(8), 2923–2939. <https://doi.org/10.1175/JCLI-D-20-0166.1>
- Illig, S. (2024). Archived data and model outputs for JGR Oceans 2024 publication on the influence of the remote equatorial dynamics on the interannual variability along the northern coast of the Gulf of Guinea [Datasets]. *Figshare*. <https://doi.org/10.6084/m9.figshare.25195445>
- Illig, S., & Bachélery, M.-L. (2019). Propagation of subseasonal equatorially-forced coastal trapped waves down to the Benguela Upwelling System. *Scientific Reports*, 9(1), 5306. <https://doi.org/10.1038/s41598-019-41847-1>
- Illig, S., & Bachélery, M.-L. (2024). The 2021 Atlantic Niño and Benguela Niño Events: External forcings and air-sea interactions. *Climate Dynamics*, 62(1), 679–702. <https://doi.org/10.1007/s00382-023-06934-0>
- Illig, S., Bachélery, M.-L., & Cadier, E. (2018). Subseasonal coastal-trapped wave propagations in the southeastern Pacific and Atlantic Oceans: 2. Wave characteristics and connection with the equatorial variability. *Journal of Geophysical Research: Oceans*, 123(6), 3942–3961. <https://doi.org/10.1029/2017JC013540>
- Illig, S., Bachélery, M. L., & Lübbecke, J. F. (2020). Why do Benguela Niños lead Atlantic Niños? *Journal of Geophysical Research: Oceans*, 125(9), e2019JC016003. <https://doi.org/10.1029/2019JC016003>
- Illig, S., Cadier, E., Bachélery, M.-L., & Kersalé, M. (2018). Subseasonal coastal-trapped wave propagations in the Southeastern Pacific and Atlantic Oceans: 1. A new approach to estimate wave amplitude. *Journal of Geophysical Research: Oceans*, 123(6), 3915–3941. <https://doi.org/10.1029/2017JC013539>
- Illig, S., Dewitte, B., Ayoub, N., du Penhoat, Y., Reverdin, G., Mey, P. D., et al. (2004). Interannual long equatorial waves in the tropical Atlantic from a high-resolution ocean general circulation model experiment in 1981–2000. *Journal of Geophysical Research*, 109(C2), C02022. <https://doi.org/10.1029/2003JC001771>
- Illig, S., Gushchina, D., Dewitte, B., Ayoub, N., & du Penhoat, Y. (2006). The 1996 equatorial Atlantic warm event: Origin and mechanisms. *Geophysical Research Letters*, 33(9), L09701. <https://doi.org/10.1029/2005GL025632>
- Imbol Koungue, R. A., Illig, S., & Rouault, M. (2017). Role of interannual Kelvin wave propagations in the equatorial Atlantic on the Angola Benguela Current system. *Journal of Geophysical Research: Oceans*, 122(6), 4685–4703. <https://doi.org/10.1002/2016JC012463>
- Keenlyside, N., & Latif, M. (2007). Understanding equatorial Atlantic interannual variability. *Journal of Climate*, 20(1), 131–142. <https://doi.org/10.1175/JCLI3992.1>
- Koné, V., Lett, C., Penven, P., Bourlès, B., & Djakouré, S. (2017). A biophysical model of *S. aurita* early life history in the Northern Gulf of Guinea. *Progress in Oceanography*, 151, 83–96. <https://doi.org/10.1016/j.pocan.2016.10.008>
- Körner, M., Brand, P., Illig, S., Dengler, M., Subramaniam, A., Bachélery, M. L., & Krahmann, G. (2024). Coastal trapped waves and tidal mixing control primary production in the tropical Angolan upwelling system. *Science Advances*, 10(4), eadj6686. <https://doi.org/10.1126/sciadv.adj6686>
- Kouadio, Y. K., Djakouré, S., Aman, A., Ali, K. E., Koné, V., & Toualy, E. (2013). Characterization of the boreal summer upwelling at the Northern Coast of the Gulf of Guinea Based on the PROPAO in situ measurements network and satellite data. *International Journal of Oceanography*, 2013, 1–11. <https://doi.org/10.1155/2013/816561>
- Lamb, P. J. (1978). Large-scale Tropical Atlantic circulation patterns associated with Sub-Saharan weather anomalies. *Tellus*, 30(3), 240–251. <https://doi.org/10.1111/j.2153-3490.1978.tb00839.x>
- Lamb, P. J., & Pepler, R. A. (1992). Further case studies of tropical Atlantic surface atmospheric and oceanic patterns associated with Sub-Saharan drought. *Journal of Climate*, 5, 476–488. https://journals.ametsoc.org/view/journals/clim/5/5/1520-0442_1992_005_0476_fcsota_2_0_co_2.xml
- Large, W. G., McWilliams, J. C., & Doney, S. C. (1994). Oceanic vertical mixing: A review and a model with a nonlocal boundary layer parameterization. *Reviews of Geophysics*, 32(4), 363–403. <https://doi.org/10.1029/94RG01872>
- Lefèvre, N., Caniaux, G., Janicot, S., & Gueye, A. K. (2013). Increased CO₂ outgassing in February–May 2010 in the tropical Atlantic, following the 2009 Pacific El Niño. *Journal of Geophysical Research: Oceans*, 118(4), 1–13. <https://doi.org/10.1002/jgrc.20107>
- Longhurst, A. (1993). Seasonal cooling and blooming in tropical oceans. *Deep Sea Research Part I*, 40(11–12), 2145–2165. [https://doi.org/10.1016/0967-0637\(93\)90095-K](https://doi.org/10.1016/0967-0637(93)90095-K)
- Lübbecke, J. F. (2013). Tropical Atlantic warm events. *Nature Geoscience*, 6(1), 22–23. <https://doi.org/10.1038/ngeo1685>
- Lübbecke, J. F., Rodríguez-Fonseca, B., Richter, I., Martín-Rey Marta, M., Losada, T., Polo, I., & Keenlyside, N. S. (2018). Equatorial Atlantic variability-Modes, mechanisms, and global teleconnections. *WIREs Climate Change*, 9(4), e527. <https://doi.org/10.1002/wcc.527>
- Marin, F., Caniaux, G., Giordani, H., Bourlès, B., Gouriou, Y., & Key, E. (2009). Why were sea surface temperatures so different in the Eastern Equatorial Atlantic in June 2005 and 2006? *Journal of Physical Oceanography*, 39(6), 1416–1431. <https://doi.org/10.1175/2008JPO4030.1>
- Martín-Rey, M., & Lazar, A. (2019). Is the boreal spring tropical Atlantic variability a precursor of the Equatorial Mode? *Climate Dynamics*, 53(3–4), 2339–2353. <https://doi.org/10.1007/s00382-019-04851-9>
- Merle, J., Fieux, M., & Hisard, P. (1979). Annual signal and interannual anomalies of sea surface temperature in the eastern equatorial Atlantic Ocean. In G. Siedler, J. D. Woods, & W. Düing (Eds.), *Oceanography and surface layer meteorology in the B/C Scale* (pp. 77–101). Pergamon.
- Mohino, E., Rodríguez-Fonseca, B., Losada, T., Gervois, S., Janicot, S., Bader, J., et al. (2011). SST-forced signals on West African rainfall from AGCM simulations—Part I: Changes in the interannual modes and model intercomparison. *Climate Dynamics*, 37(9–10), 1707–1725. <https://doi.org/10.1007/s00382-011-1093-2>
- Moore, D. W. (1968). Planetary-gravity waves in an equatorial ocean. (PhD thesis). Harvard University.

- Morlière, A. (1970). Les saisons marines devant Abidjan. *Documents Scientifiques, Centre de Recherches Océanographiques, Abidjan*, 1, 2, 1–15.
- Morrow, R., Fu, L., Ardhuin, F., Benkiran, M., Chapron, B., Cosme, E., et al. (2019). Global observations of fine-scale ocean surface topography with the Surface Water and Ocean Topography (SWOT) Mission. *Frontiers in Marine Science*, 6, 433647. <https://doi.org/10.3389/fmars.2019.00232>
- Penven, P., Marchesiello, P., Debreu, L., & Lefevre, J. (2007). Software tools for pre- and post-processing of oceanic regional simulations. *Environmental Modelling & Software*, 23(5), 660–662. <https://doi.org/10.1016/j.envsoft.2007.07.004>
- Philander, S. G. H. (1990). *El Niño, La Niña, and the Southern Oscillation*. Academic Press.
- Philander, S. G. H. (1979). Upwelling in the Gulf of Guinea. *Journal of Marine Research*, 37, 23–33.
- Picaut, J. (1983). Propagation of the seasonal upwelling in the Eastern Equatorial Atlantic. *Journal of Physical Oceanography*, 13(1), 18–37. [https://doi.org/10.1175/1520-0485\(1983\)013<0018:Potsui>2.0.CO;2](https://doi.org/10.1175/1520-0485(1983)013<0018:Potsui>2.0.CO;2)
- Picaut, J., & Verstraete, J. M. (1979). Propagation of a 14.7-day wave along the northern coast of the Guinea Gulf. *Journal of Physical Oceanography*, 9(1), 136–149. [https://doi.org/10.1175/1520-0485\(1979\)009<0136:POADWA>2.0.CO;2](https://doi.org/10.1175/1520-0485(1979)009<0136:POADWA>2.0.CO;2)
- Polo, I., Lazar, A., Rodríguez-Fonseca, B., & Arnault, S. (2008). Oceanic Kelvin waves and tropical Atlantic intraseasonal variability: 1. Kelvin wave characterization. *Journal of Geophysical Research*, 113(C7), C07009. <https://doi.org/10.1029/2007JC004495>
- Pujol, M.-I., Faugère, Y., Taburet, G., Dupuy, S., Pelloquin, C., Ablain, M., & Picot, N. (2016). DUACS DT2014: The new multi-mission altimeter data set reprocessed over 20 years. *Ocean Science*, 12(5), 1067–1090. <https://doi.org/10.5194/os-12-1067-2016>
- Ridgway, K. R., Dunn, J. R., & Wilkin, J. L. (2002). Ocean interpolation by four-dimensional least squares—Application to the waters around Australia. *Journal of Atmospheric and Oceanic Technology*, 19(9), 1357–1375. [https://doi.org/10.1175/1520-0426\(2002\)019<1357:oibfdw>2.0.co;2](https://doi.org/10.1175/1520-0426(2002)019<1357:oibfdw>2.0.co;2)
- Rodríguez-Fonseca, B., Mohino, E., Mechoso, C. R., Caminade, C., Biasutti, M., Gaetani, M., et al. (2015). Variability and predictability of West African droughts: A review on the role of sea surface temperature anomalies. *Journal of Climate*, 28(10), 4034–4060. <https://doi.org/10.1175/JCLI-D-14-00130.1>
- Rouault, M., Illig, S., Bartholomae, C., Reason, C. J. C., & Bentamy, A. (2007). Propagation and origin of warm anomalies in the Angola Benguela upwelling system in 2001. *Journal of Marine Systems*, 68(3–4), 473–488. <https://doi.org/10.1016/j.jmarsys.2006.11.010>
- Rouault, M., Illig, S., Lübbecke, J., & Imbol Koungue, R. A. (2018). Origin, development and demise of the 2010–2011 Benguela Niño. *Journal of Marine Systems*, 188, 39–48. <https://doi.org/10.1016/j.jmarsys.2017.07.007>
- Ruiz-Barradas, A., Carton, J. A., & Nigam, S. (2000). Structure of interannual-to-decadal climate variability in the tropical Atlantic sector. *Journal of Climate*, 13(18), 3285–3297. [https://doi.org/10.1175/1520-0442\(2000\)013<3285:SOITDC>2.0.CO;2](https://doi.org/10.1175/1520-0442(2000)013<3285:SOITDC>2.0.CO;2)
- Sciremammano, F. (1979). A suggestion for the presentation of correlations and their significance levels. *Journal of Physical Oceanography*, 9(6), 1273–1276. [https://doi.org/10.1175/1520-0485\(1979\)009<1273:asftpo>2.0.co;2](https://doi.org/10.1175/1520-0485(1979)009<1273:asftpo>2.0.co;2)
- Servain, J., Wainer, I., Ayina, H. L., & Roquet, H. (2000). The relationship between the simulated climate variability modes of the tropical Atlantic. *International Journal of Climatology*, 20(9), 939–953. [https://doi.org/10.1002/1097-0088\(200007\)20:9<939::AID-JOC511>3.0.CO;2-V](https://doi.org/10.1002/1097-0088(200007)20:9<939::AID-JOC511>3.0.CO;2-V)
- Sohou, Z., Koné, V., Da-Allada, Y. C., Djakouré, S., Bourlès, B., Racape, V., et al. (2020). Seasonal and inter-annual ONSET Sea Surface Temperature variability along the northern coast of the Gulf of Guinea. *Regional Studies in Marine Science*, 35, 101129. <https://doi.org/10.1016/j.rsma.2020.101129>
- Tomety, F. S., Illig, S., Ostrowskiy, M., Awo, F. M., Bachèlery, M.-L., Keenlyside, N., & Rouault, M. (2024). Long-term climatological trends driving the recent warming along the Angolan and Namibian coasts. *Climate Dynamics*, 2024, 1–20. <https://doi.org/10.1007/s00382-024-07305-z>
- Topé, G. D. A., Alory, G., Djakouré, S., Da-Allada, C. Y., Jouanno, J., & Morvan, G. (2023). How does the Niger River warm coastal waters in the Northern Gulf of Guinea? *Frontiers in Marine Science*, 10, 1187202. <https://doi.org/10.3389/fmars.2023.1187202>
- Toualy, E., Stanojevic, G., Kouadio, K. Y., & Aman, A. (2012). Multi-decadal variability of sea surface temperature in the Northern Coast of Gulf of Guinea. *Asian Journal of Applied Sciences*, 5(8), 552–562. <https://doi.org/10.3923/ajaps.2012.552.562>
- Varlet, F. (1958). Les traits essentiels du régime côtier de l'Atlantique près d'Abidjan (Côte d'Ivoire). *Bulletin de l'IFAN: Sciences Naturelles*, 20A, 1089–1102.
- Vizy, E. K., & Cook, K. H. (2001). Mechanisms by which Gulf of Guinea and eastern North Atlantic sea surface temperature anomalies can influence African rainfall. *Journal of Climate*, 14(5), 795–821. [https://doi.org/10.1175/1520-0442\(2001\)014<0795:mbwgog>2.0.co;2](https://doi.org/10.1175/1520-0442(2001)014<0795:mbwgog>2.0.co;2)
- Xie, S.-P., & Carton, J. A. (2004). Tropical Atlantic variability: Patterns, mechanisms, and impacts. In C. Wang, S.-P. Xie, & J. A. Carton (Eds.), *Earth's climate: The ocean-atmosphere interaction, Geophysical monograph series* (pp. 121–142). American Geophysical Union.
- Zebiak, S. E. (1993). Air–sea interaction in the equatorial Atlantic region. *Journal of Climate*, 6(8), 1567–1586. [https://doi.org/10.1175/1520-0442\(1993\)006<1567:AIITEA>2.0.CO;2](https://doi.org/10.1175/1520-0442(1993)006<1567:AIITEA>2.0.CO;2)

References From the Supporting Information

- Okumura, Y., & Xie, S. (2006). Some overlooked features of tropical Atlantic climate leading to a new Niño-like phenomenon. *Journal of Climate*, 19(22), 5859–5874. <https://doi.org/10.1175/JCLI3928.1>
- Taylor, K. E. (2001). Summarizing multiple aspects of model performance in a single diagram. *Journal of Geophysical Research*, 106(D7), 7183–7192. <https://doi.org/10.1029/2000jd900719>

Supporting Information for

“Influence of the remote equatorial dynamics on the interannual variability along the northern coast of the Gulf of Guinea”

Serena Illig^{1,2}, Sandrine Djakouré³, Toussaint Mitchodigni^{4,5}

¹ Laboratoire d'Etudes en Géophysique et Océanographie Spatiale (LEGOS), CNRS/IRD/UT3/CNES, Toulouse, France. serena.illig@ird.fr

² Department of Oceanography, University of Cape Town, Cape Town, Rondebosch, South Africa.

³ Laboratory of Matter, Environmental and Solar Energy Sciences (LASMES), Ocean-Atmosphere Interaction Group, University Félix Houphouët-Boigny, 22 BP 582 Abidjan 22, Côte d'Ivoire

⁴ Department of Oceanography and Applications, International Chair in Mathematical Physics and Applications, University of Abomey-Calavi, Cotonou, Benin.

⁵ Institut de Recherches Halieutiques et Océanologiques du Bénin, Cotonou, Benin

Submitted to *Journal of Geophysical Research - Oceans* in February 2024

S1. Validation of CROCO^{REF} interannual variability

The model interannual Sea Level Anomalies (SLA) are compared to the AVISO daily altimeter satellite gridded product over the period 1993-2015. The AVISO SLA is estimated by optimal interpolation by merging the L3 along-track measurement from the different altimeter missions available on a $1/4^\circ \times 1/4^\circ$ Mercator grid (Pujol et al. 2016). This product is processed by the DUACS multi-mission altimeter data processing system and distributed by the Copernicus marine data store (<https://data.marine.copernicus.eu>).

We use the daily global OISST product (version 2) blended with AVHRR data, (also known as Reynolds_AVHRR'SST, Huang et al. 2021) to evaluate of the model interannual SST anomalies (SSTA) over the period 1982-2015. This product merges SST observations from remotely sensed AVHRR observations and *in situ* platforms (ships and buoys). The latter are interpolated onto a 0.25° grid and extrapolated using Optimal Interpolation at the NOAA

National Centers for Environmental Information. Data were downloaded from the <http://apdrc.soest.hawaii.edu> data server.

The model mean state, seasonal, and interannual variability has been extensively validated in the southeastern Atlantic in Illig et al. (2020) for the study of the phenology of the Atlantic and Benguela Niño extreme events. Here, we focus our analysis on the key parameters related to the ocean dynamics relevant for our study, i.e. the surface interannual fluctuations in the east-equatorial Atlantic and along the NGG coast.

The realism of the CROCO^{REF} interannual variability along the equatorial and NGG coastal waveguides is examined in **Fig.A1** and **Fig.A2**. For a complete description of the methodology used to calculate the interannual anomalies, please refer to **section 2.2** of the manuscript. **Fig.A1a** illustrates the good coherence between the CROCO^{REF} interannual SLA and the AVISO altimetric observations from 1993 to 2015 in the eastern equatorial sector (KATL box, black lines) and along the NGG coast off Benin-Togo (BT box, maroon lines) and off eastern Côte d'Ivoire (CI, blue lines). The model reproduces the sequence of warm and cold events remarkably well, in particular the extreme SLA in the boreal spring of 1996 and the lowest SLA values in early 2012.

The comparison between model and altimetry shows highly significant correlations of 0.79, 0.67, and 0.67 in the KATL, BT, and CI domains, respectively. The amplitude of the model interannual SLA is also in very good agreement with the observations, with model-to-observations standard deviation ratios of 1.01, 0.90, and 0.99 in KATL, BT, and CI, respectively (cf. black, maroon, and blue open squares in **Fig.A1b**). **Fig.A1b** further presents the model/observations comparison for interannual SLA time series along the 1°-wide path of the equatorial (from 20°W to 8°E) and NGG coastal waves using a Taylor diagram (Taylor, 2001). The color of the dots represents the distance from [0°E; 0°N], as shown in **Fig.1a** of the manuscript. Along the equatorial waveguide (distance<1000km), the results show a very good agreement between model and altimetric data, with an accurate estimate of the magnitude of the interannual variability and correlations well above the 99% confidence level (Sciremammano, 1979), leading to Taylor scores (see Eq.4 of Taylor, 2001) above 0.85. Along the NGG coast, interannual SLA are also in very good agreement with observations, with Taylor scores above 0.7. Of particular interest is the seasonal modulation of the interannual SLA variability, shown in **Fig.A1c**. The results show that the level of interannual variability in the KATL, BT, and CI boxes is in good agreement with the observations. The model realistically simulates the enhanced east-equatorial variability in the boreal spring and summer (season of the Atlantic Niño events, Lübbecke et al. 2018) and the small secondary peak of variability in October-November (season of the Atlantic Niño II, Okumura and Xie, 2006). Along the NGG coast, there are also two seasons with increased SLA interannual variability, spring and fall. CROCO^{REF} overestimates the second peak of variability off Benin-Togo, while it underestimates it off Côte d'Ivoire. This discrepancy between model and observations may be due to a seasonal bias in the model coastal stratification, or it may be related to a lack of altimetric observations in the coastal band and the large interpolation radii (Pujol et al. 2016).

The ability of CROCO^{REF} to simulate the observed interannual SST fluctuations is assessed in **Fig.A2a** for the KATL, BT, and CI domains over the period 1982-2015. Along the eastern equatorial waveguide, the results show that the model agrees remarkably well with the observations, both in terms of amplitude and coherence, with a Taylor score of 0.93 in KATL

(cf. open black square **Fig.A2b**). Along the NGG coast, the model reproduces the observed sequence of warm and cold events, but overestimates the magnitude of the interannual variability, especially off western Côte d'Ivoire. The Taylor diagram shown in **Fig.A2b** confirms the realism of the interannual SST variations along the equatorial and coastal waveguides, with statistically significant correlations and Taylor scores greater than 0.60. The seasonal modulation of the equatorial and coastal interannual variability (**Fig.A2c**) is in very good agreement with the observations, with the variability in the CI box being overestimated throughout the year compared to the observations. However, this validation exercise remains challenging, because remotely sensed L3 products do not include much coastal data and gridding processes tend to smooth coastal gradients.

In conclusion, the overall good agreement between CROCO^{REF} and observations implies that the equatorial and coastal dynamics are adequately simulated by our model configuration. This gives confidence to analyze the connection between equatorial and coastal interannual variability in the GoG and to perform sensitivity experiments to disentangle the effect of remote equatorial forcing from the variability driven by local atmospheric forcing.

S2. Composite of CROCO^{REMOTE} sensitivity experiment

Fig.B shows the composite analysis of the CROCO^{REMOTE} sensitivity experiments in which the interannual surface forcing in the eastern GoG and along the NGG coast has been filtered out, in favor of the remotely-forced coastal variability (see **Section 2.3**).

The composites combine the most energetic equatorial interannual propagations, identified when the KATL SLA exceeds 1.5 times the STD in both CROCO^{REF} and CROCO^{REMOTE}. Based on this criterion, we selected 30 strong equatorial propagations (15 downwelling and 15 upwelling), shown as red and blue dots in **Fig.2a** and **Fig.Ba**.

Figures Bb-d and **2b-d** show that these strong rises and falls in the KATL SLA are consistent with the wind-forced linear wave dynamics, with a clear signature of eastward-propagating equatorial Kelvin waves, their reflection into equatorial Rossby waves, and evidence of coastal trapped wave propagation along the NGG coastline. Comparison of **Figs Bb-d** and **2b-d** allows to assess the averaged effect of the interannual coastal surface forcing on the connection between the equatorial and coastal variability. The results and their limitations are discussed in **section 3.2**.

S3. Result of $\widetilde{\text{EXP}}$ in the KATL box

Fig.C shows the results of the $\widetilde{\text{EXP}}$ idealized experiments (see **Section 2.3**) in the eastern equatorial Atlantic (KATL box). The experiments consist of the ocean response to a wind-stress perturbation, applied sequentially in each month of the year, triggering a downwelling EKW that propagates over a seasonally-varying ocean mean state. **Fig.Cbc** are presented here for the sake of completeness but are very similar to **Figure 8ab** of Illig et al. (2020). Seasonal modulation of the amplitude and timing of the KATL SLA and SSTA are useful for analyzing the results obtained along the NGG coast, in the BT and CI boxes.

References

- Huang, B., C. Liu, V. Banzon, E. Freeman, G. Graham, B. Hankins, T. Smith, and H.-M. Zhang (2021). Improvements of the Daily Optimum Interpolation Sea Surface Temperature (DOISST) Version 2.1. *J. Climate*, 34(8), 2923–2939. DOI: 10.1175/JCLI-D-20-0166.1.
- Illig, S., M. L. Bachèlery, and J. F. Lübbecke (2020). Why do Benguela Niños lead Atlantic Niños?, *J. Geophys. Res. Oceans*, 125(9), e2019JC016003, doi:<https://doi.org/10.1029/2019JC016003>.
- Pujol, M.-I., Faugère, Y., Taburet, G., Dupuy, S., Pelloquin, C., Ablain, M., and Picot, N.: DUACS DT2014: the new multi-mission altimeter data set reprocessed over 20 years, *Ocean Sci.*, 12, 1067–1090, <https://doi.org/10.5194/os-12-1067-2016>, 2016.
- Okumura, Y., & Xie, S. (2006). Some overlooked features of tropical Atlantic climate leading to a new Niño-like phenomenon. *Journal of Climate*, 19(22), 5859–5874. <https://doi.org/10.1175/JCLI3928.1>.
- Taylor, K. E. (2001). Summarizing multiple aspects of model performance in a single diagram. *Journal of Geophysical Research*, 106, 7183–7192.

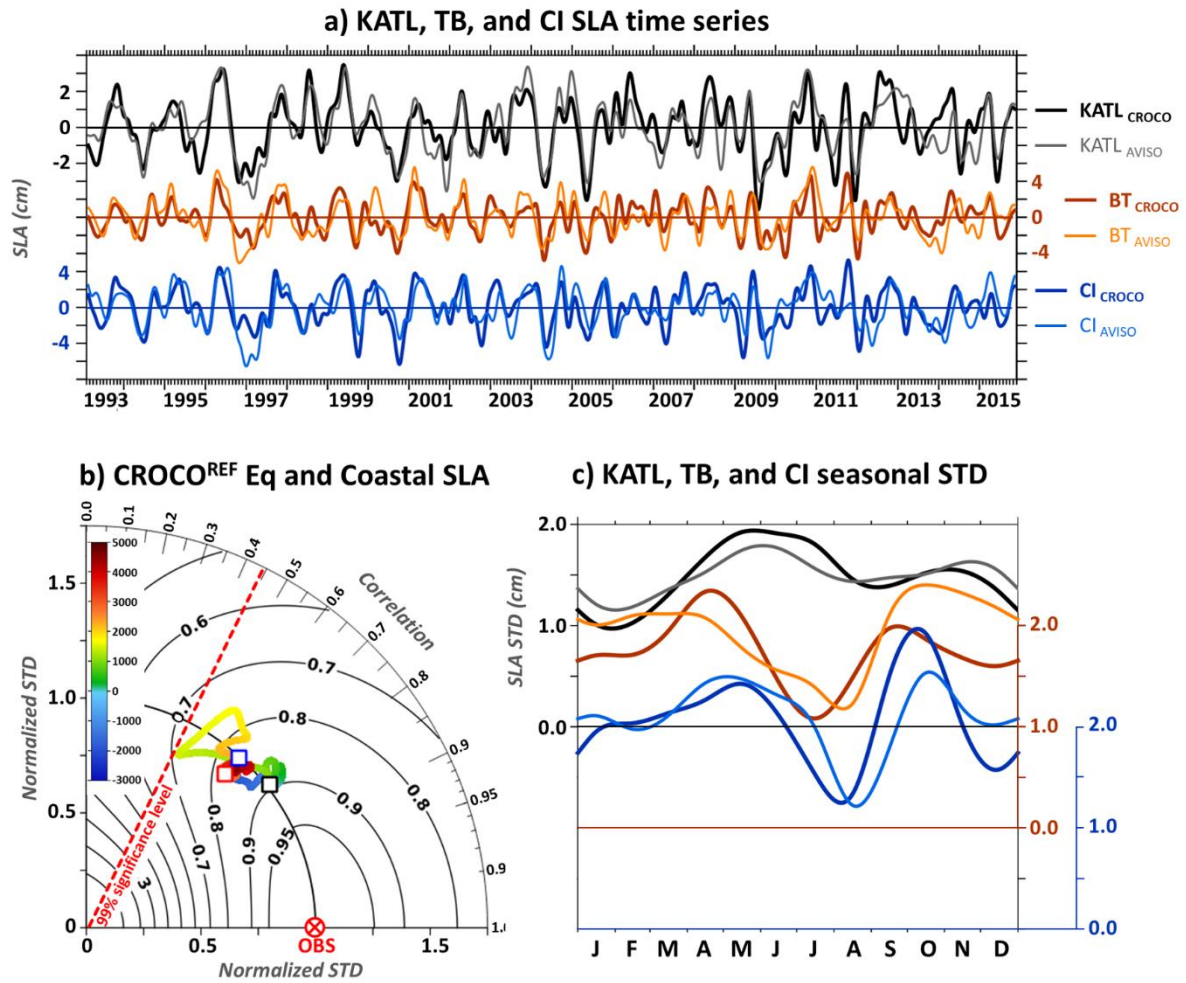


Figure S1: Comparison between CROCO^{REF} interannual SLA variability and AVISO altimetric data over the period 1993-2015. **a)** Interannual SLA (in cm) averaged in KATL ([20°W-0°E; 0.5°S-0.5°N], black lines, left scale), BT ([1°E-3°E; 1°-wide coastal margin], maroon lines, right scale), and CI ([5°W-3°W; 1°-wide coastal margin], blue lines, blue left scale) boxes for CROCO^{REF} outputs (thick lines) and observations (thin lines). **b)** Normalized Taylor diagram (Taylor, 2001) illustrating CROCO^{REF} skills in representing the interannual altimetric SLA variability along of the 1°-wide path of equatorial (from 20°W to 8°E) and coastal wave propagations. Colors indicate the distance (in km) from [0°E; 0°N], similar to **Fig.1a**. Black, maroon, and blue open squares are for the KATL, BT, and CI indices, respectively. Isolines provide a measure of the skill as defined by equation (4) from Taylor (2001). The dashed radius line indicates the limit of the 99% significance level for the correlation (Sciremammano, 1979). **c)** Monthly climatology of the interannual SLA STD (cm) in KATL (black lines, left scale), BT (maroon lines, maroon right scale), and CI (blue lines, blue right scale) boxes for CROCO^{REF} outputs (thick lines) and observations (thin lines).

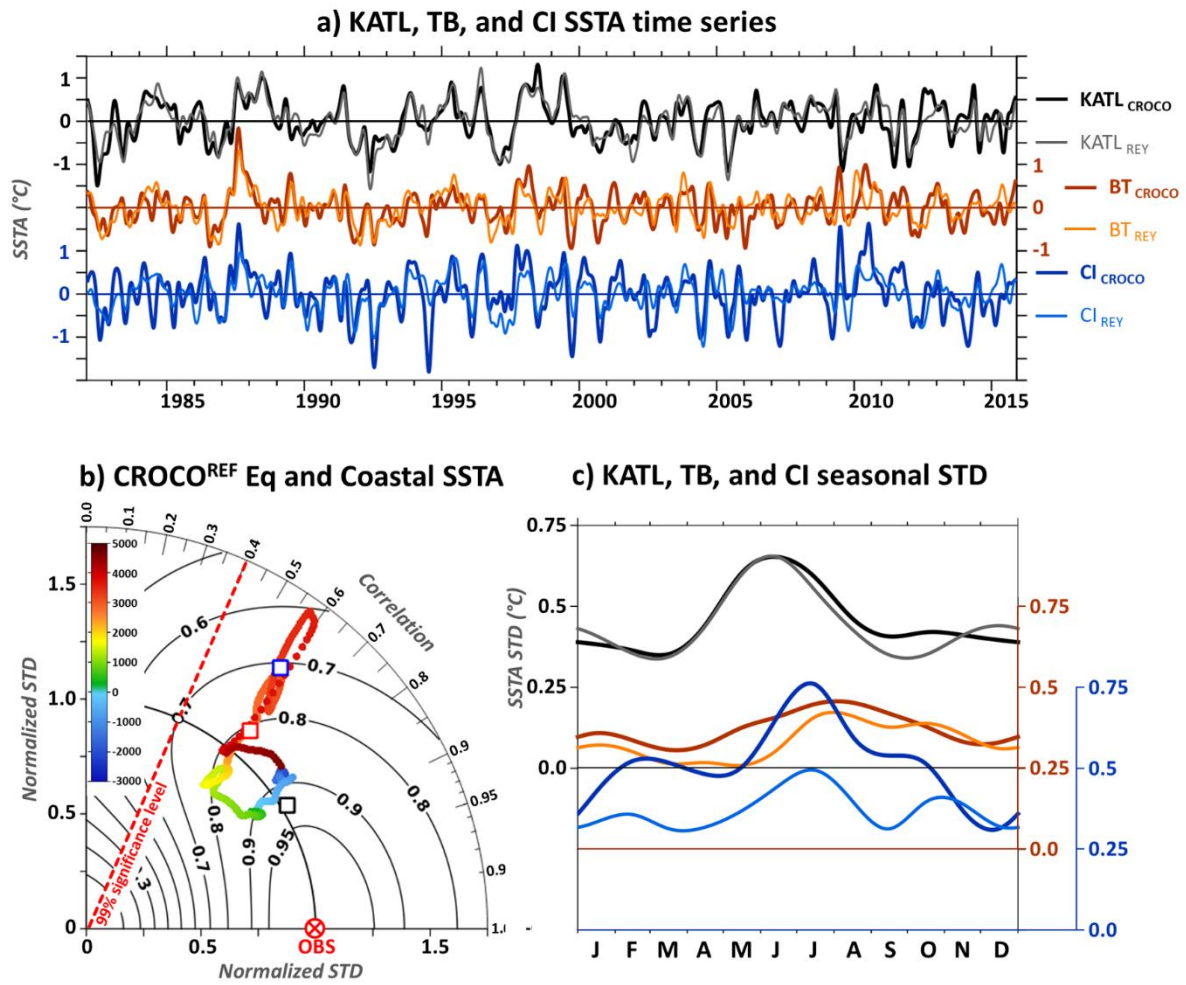


Figure S2: Same as **Fig.A1** but for the validation of CROCO^{REF} interannual SST variability (in °C) compared to the remote-sensed Reynolds data over the period 1982-2015.

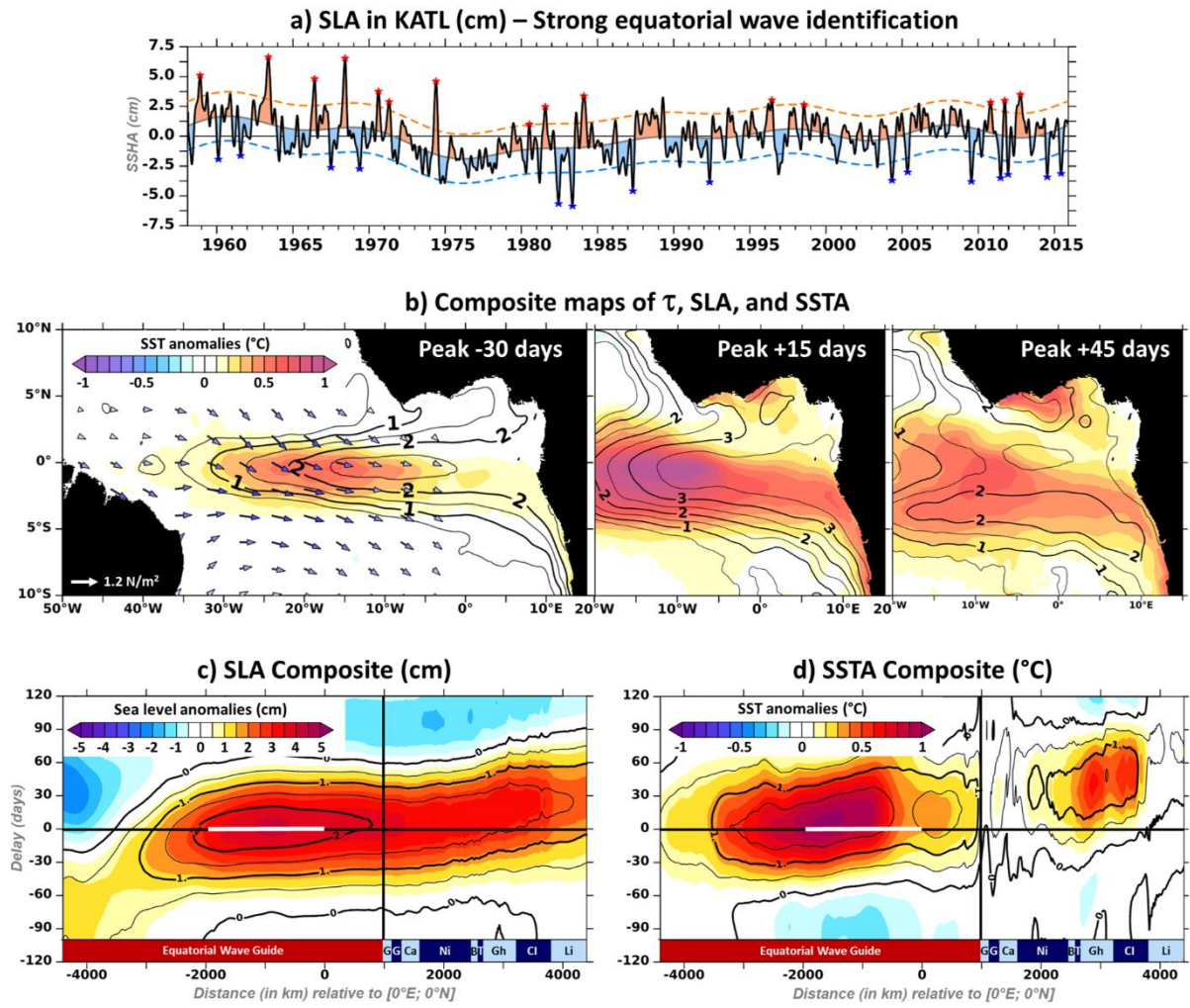


Figure S3: Same as **Fig.2** but for the composite of the CROCO^{REMOTE} sensitivity experiment, in which the interannual surface forcing in the eastern Gulf of Guinea and along the NGG coast has been filtered-out.

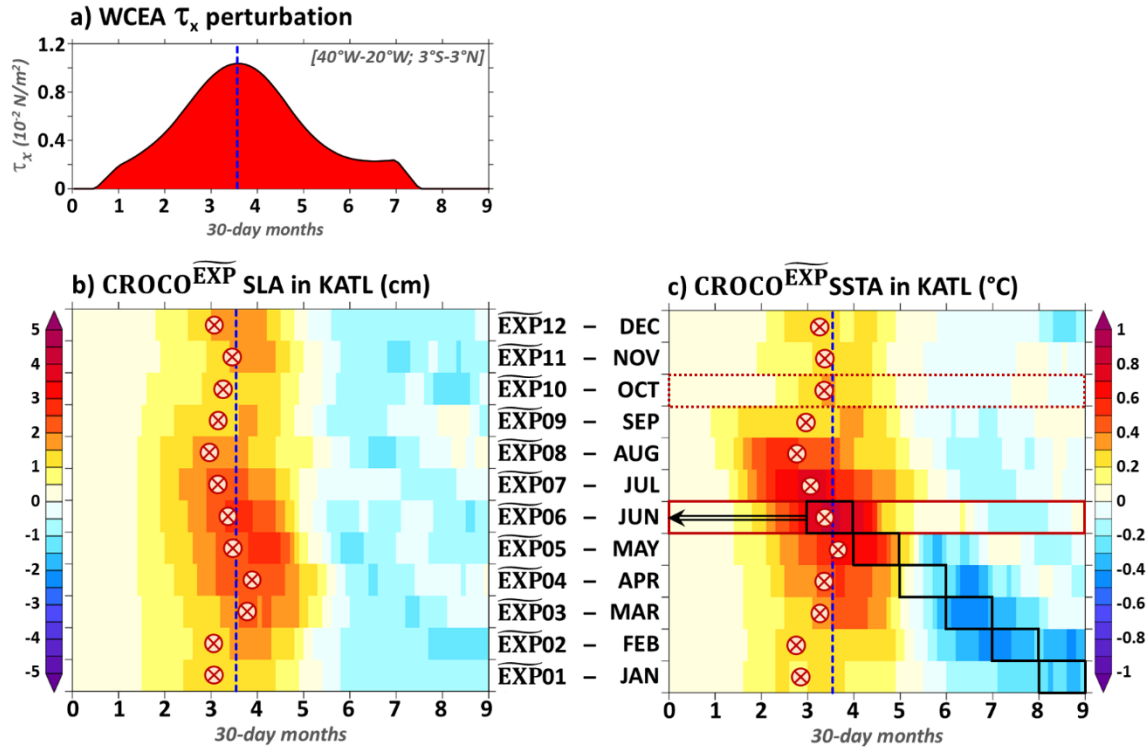


Figure S4: a) Timeseries of the zonal wind-stress perturbations (10^{-2} N/m^2) averaged in the western-central equatorial Atlantic ($[40^\circ\text{W}-20^\circ\text{W}; 3^\circ\text{S}-3^\circ\text{N}]$). **bc)** Same as **Fig.5ab** for the KATL box. Black rectangles in panel c show the month of June associated with each $\widehat{\text{EXP}}$ experiment.